Aberrant youth: Chemical and isotopic constraints on the origin of off-axis lavas from the East Pacific Rise, 9°–10°N

K. W. W. Sims

Department of Geology and Geophysics, Woods Hole Oceanographic Institution, MS #22 Woods Hole Road, Woods Hole, Massachusetts 02543, USA (ksims@whoi.edu)

J. Blichert-Toft

Laboratoire des Sciences de la Terre, CNRS UMR 5570, Ecole Normale Superieure de Lyon 46, Allee d'Italie, 69364 Lyon Cedex 7, France (jblicher@ens-lyon.fr)

D. J. Fornari

Department of Geology and Geophysics, Woods Hole Oceanographic Institution, MS #22 Woods Hole Road, Woods Hole, Massachusetts 02543, USA (dfornari@whoi.edu)

M. R. Perfit

Department of Geological Sciences, University of Florida, 241 Williamson Hall, P.O. Box 112120, Gainesville, Florida 32611–2120, USA (perfit@geology.ufl.edu)

S. J. Goldstein

Group C-INC, Isotope and Nuclear Chemistry, Los Alamos National Laboratory MS J514, Los Alamos, New Mexico 87545, USA (sgoldstein@lanl.gov)

P. Johnson

Hawaii Mapping Research Group, University of Hawaii, SOEST, Honolulu, Hawaii 96822, USA (pjohnson@soest.hawaii.edu)

D. J. DePaolo

Center for Isotope Geochemistry, Earth and Planetary Science Department MC4767, University of California, Berkeley, California 94720–4767, USA (depaolo@eps.berkeley.edu)

S. R. Hart

Department of Geology and Geophysics, Woods Hole Oceanographic Institution, MS #22 Woods Hole Road, Woods Hole, Massachusetts 02543, USA (shart@whoi.edu)

M. T. Murrell

Group C-INC, Isotope and Nuclear Chemistry, Los Alamos National Laboratory MS J514, Los Alamos, New Mexico 87545, USA (mmurrell@lanl.gov)

P. J. Michael

Department of Geosciences, University of Tulsa, 600 S. College Avenue, Tulsa, Oklahoma 74104, USA (pjm@utulsa.edu)

G. D. Layne

Department of Geology and Geophysics, Woods Hole Oceanographic Institution, MS #22 Woods Hole Road, Woods Hole, Massachusetts 02543, USA (glayne@whoi.edu)

L. A. Ball

Department of Marine Chemistry and Geochemistry, Woods Hole Oceanographic Institution, Woods Hole Road, Woods Hole, Massachusetts 02543, USA (lball@whoi.edu)

[1] We report measurements of U-series disequilibria, Sr, Nd, Hf, and Pb isotopic compositions and major and trace element abundances in a suite of well-located, off-axis MORBs that span the East Pacific Rise (EPR) ridge crest from 9°48′–52′N and across it for ~4 km on either side. The geological context of the samples are well constrained as they were collected by submersible in an area that has been extensively imaged by remote sensing techniques. Sr, Nd, Hf and $^{208}Pb/^{206}Pb$ isotopic compositions of the off-axis N-MORB are identical to the axial lavas from this same region, suggesting that their sources are similar and that melting processes are the dominant influence in establishing the U-Th-Ra disequilibria and trace element fractionations. A majority of off-axis samples have U-Th and Th-Ra disequilibria that are larger, and model ages that are younger, than would be predicted from their off-axis distance and the time-integrated spreading rate. There are, however, a few off-axis samples with U-Th ages that are consistent with their spreading rate ages. It is likely that these samples erupted within or close to the axial summit trough (AST) and aged at a rate proportional to the spreading rate. The anomalously young ages determined for most of the off-axis lavas suggest that volcanic construction along this region is occurring over a zone that is wider (at least 4 km) than the AST (10s to 100s of meters). The combined observational, chemical and isotopic data support a model for the 9°0′N area that includes a significant component of crustal accumulation resulting from lavas that breach the AST and flow down the flanks of the EPR ridge crest. However, these data also require a minor component of off-axis eruptions that occur on distinct pillow mounds and ridges. This suggests that MOR construction involves several volcanic and tectonic processes acting in concert to form a complex patchwork of lava ages and compositions along, and across, this fast spreading ridge crest.

———————————

Theme: The Oman Ophiolite and Mid-Ocean Ridge Processes
Guest Editors: Peter Kelemen, Chris MacLeod, and Susumu Umino

1. Introduction

[2] The fast spreading East Pacific Rise (EPR), from 9°–10°N, is one of the most intensively sampled sites along the world's mid-ocean ridges, with over 1200 rock samples collected via rock core, dredge and submersible [*Batiza and Niu*, 1992; *Perfit et al.*, 1994; *Perfit and Chadwick*, 1998; *Smith et al.*, 2001, and references therein].

Although geological mapping, qualitative age constraints and remote sensing data suggest much of the recent volcanic activity along 9°–10°N EPR has been largely confined to the narrow axial summit trough (AST) [e.g., *Haymon et al.*, 1991; *Fornari et al.*, 1998; *Perfit and Chadwick*, 1998; *Schouten et al.*, 2001], three key observations indicate that volcanic construction along this section of the EPR may actually occur over a zone

that is considerably wider than the AST: (1) Recent seismic studies suggest that seismic layer 2A, inferred to be the extrusive crust, doubles in thickness away from the AST, over a region up to several kilometers wide [*Christeson et al.*, 1994; 1996; *Harding et al.*, 1993; *Vera and Diebold*, 1993; *Schouten et al.*, 1999, 2001]; (2) Off-axis observations during submersible dives have documented flows and pillow mounds that appear to be younger than the surrounding lavas [*Macdonald et al.*, 1996; *Perfit et al.*, 1994; *Perfit and Chadwick*, 1998]; (3) U-series model eruption ages have identified basalts located up to 4 km from the AST that are younger than would be inferred from crustal spreading rates [*Goldstein et al.*, 1992, 1993, 1994].

[3] Two models of crustal genesis have been proposed to explain the observed off-axis thickening of the extrusive section of the oceanic crust (i.e., seismic layer 2A) and the existence of anomalously young ages for off-axis basalts. One model suggests the extrusive crust is being built by frequent small volume flows confined largely within the AST and less frequent large flows that breach the AST and flow off-axis for several kilometers through surface channels or subsurface conduits [*Hooft et al.*, 1996]. The other model proposes that small volume flows, with distinct compositions and sources, erupt off-axis along ridge-parallel fissures and faults [*Perfit et al.*, 1994; *Goldstein et al.*, 1992, 1994; *White et al.*, 2002; *Reynolds and Langmuir*, 2000].

[4] While off-axis volcanism has been inferred to be an important component in the construction of the 9°–10°N EPR crustal section [*Christeson et al.*, 1992, 1994, 1996; *Harding et al.*, 1993; *Perfit et al.*, 1994; *Goldstein et al.*, 1994], a lack of constraints on the ages and isotopic compositions of off-axis lavas has resulted in uncertainty regarding the temporal and genetic context of off-axis magmatism. Here, we present U-Th-Ra disequilibria results in conjunction with elemental data and Sr, Nd, Hf, and Pb isotopic compositions for 14 samples selected from a large, two-dimensional suite of off-axis MORB that span the ridge crest between 9° 48′–52′N for ∼4 km on both sides of the axis. Two important aspects of this

study should be noted. First, the geological context of the samples are well constrained; the samples were collected by submersible in an area that has now been extensively imaged by remote sensing techniques including side-scan sonar, high resolution altimetric data, and deep sea photography [*Fornari et al.*, 1998; *Kurras*, 2000; *Schouten et al.*, 2001, 2002]. Second, we have comprehensively characterized young, axial basalts from the most recently active portion of the 9°–10°N EPR segment in terms of major and trace element compositions, U-Th-Ra and U-Pa disequilibria and Sr, Nd, Hf, and Pb isotopic compositions [*Sims et al.*, 2002]. This baseline reference combined with our knowledge of the geological context of the off-axis lavas enables us to evaluate whether the unusually "young" off-axis lavas were erupted from vents/fissures off-axis, or whether instead they were erupted within, or proximal to, the AST, and flowed for considerable distances (kilometers) down the axial high through lava tubes and/or surface channels. Furthermore, knowing the chemical and isotopic compositions of the axial lavas further allows us to use the U-Th-Ra disequilibria data to constrain the extent and timing of off-axis volcanism and to contrast the chemistries of the axial and off-axis lavas in order to compare their sources and genetic histories.

2. Sample Locations and Geological Setting of Off-Axis Lavas

[5] The EPR, between 9°–10° N, (Figure 1) is defined as a "second-order" spreading segment bounded to the north by the Clipperton Transform Fault, and to the south by the large overlapping spreading center (OSC) at 9°03′N. This EPR segment is a fast spreading ridge (full spreading rate of 110 mm/yr), which paleomagnetic data indicate has been spreading at a constant rate over the past 2 Ma [*Carbotte and Macdonald*, 1992]. The continuity of the EPR axis along this segment is interrupted at 9°37′N [*Langmuir et al.*, 1986] by a small overlapping spreading center that has acted as a hydrothermal and volcanological divide between the 9° 03′N OSC and the Clipperton transform [see *Smith et al.*, 2001, and references therein].
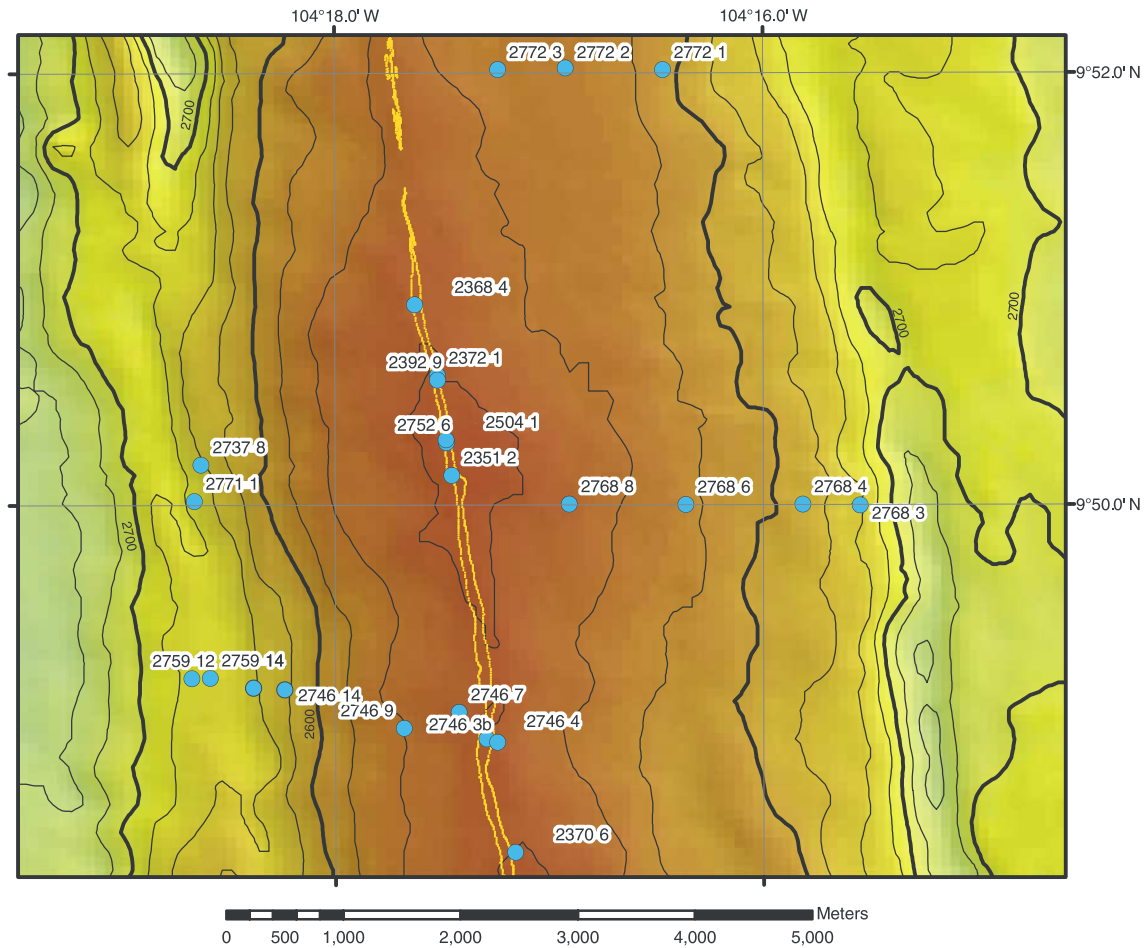
Figure 1. (a) Multibeam bathymetric map; 25 meter contour intervals. Yellow line is trace of AST based on 100 kHz side-scan sonar data collected in 1989 [*Haymon et al.*, 1991; *Fornari et al.*, 1998]. (b) Side-scan sonar image of the EPR crest from 9°48′–9°50′N EPR [*Schouten et al.*, 2002]. This area has a narrow AST (<100 m wide and <15 m deep). Young lobate and sheet lavas, which sometimes terminate in pillowed flow fronts, dominate the flanks of the ridge crest adjacent to the AST. In plan view these lavas appear to interfinger and override each other forming a convex outward "shingled" appearance out to about 1–2 km. Beyond this distance there are distinct pillow mounds and ridges up to ~20 m high (some of these are outlined in red), located several kilometers off-axis, which do not appear to have been sourced from lava flows erupted within or adjacent to the AST. Symbols showing sample locations are colored according to their MgO content (see key).

[6] The focus of our study is the northern region of this segment, from 9°48′–52′N. In the 9°48′–52′N region (hereafter called the 9°50′N region) of the EPR, the thickness of seismic layer 2A, increases from ~300 m at the ridge axis to ~600 m at ~2 km off-axis [*Christeson et al.*, 1994, 1996; *Harding et al.*, 1993; *Vera and Diebold*, 1994; *Schouten et al.*, 1999, 2001, 2002]. On the basis of analysis of multibeam bathymetry and other parameters this region appears to be the most magmatically robust region of the 9°–10°N segment [*Macdonald and Fox*, 1988; *Scheirer and Macdonald*, 1993]. In

cross-section, the ridge crest along 9°48′–52′N is a broad axial high, 2–5 kilometers wide, bisected by the axial summit trough (AST) [*Fornari et al.*, 1998]. The AST is a narrow trough, 10 to 100 m wide and 10 to 50 m deep, and is the locus of focused volcanism and hydrothermal activity along the ridge crest. Volcanism in the AST is characterized by sheet flows, lava ponds and drain back features [*Haymon et al.*, 1991, 1993; *Fornari et al.*, 1998; *Perfit and Chadwick*, 1998]. Off-axis the surface morphology and structural features change across the ridge crest, creating two distinct off-axis
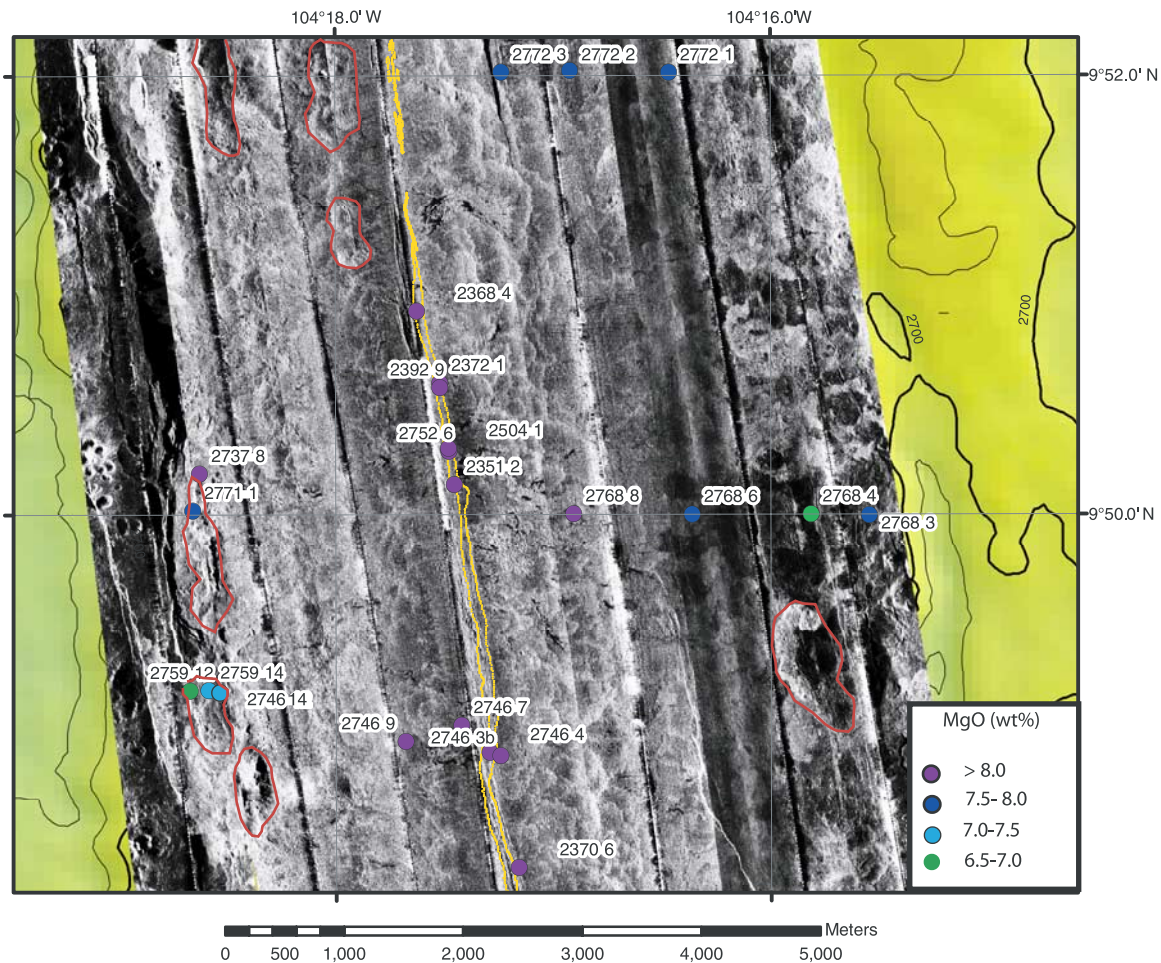
Figure 1. (continued)

geological regimes. Adjacent to the AST, the surface morphology is dominated by magmatic/volcanic processes, whereas further off-axis tectonic processes become more dominant. Recent 120 kHz side-scan sonar imagery (Figure 1b), high resolution micro-bathymetry and deep sea photographic transects of the ridge crest in our study area indicate that the 9°–10°N EPR crest is dominated by scalloped acoustic reflectors that are inferred to be lava flow surfaces and flow fronts [*Fornari et al.*, 1998; *Kurras et al.*, 2000; *Scheirer et al.*, 2000; *Schouten et al.*, 2001, 2002]. This is primarily evident in the near axis terrain from 9°55′N down to 9°27′N, and extending outward from the axial trough to variable distances, usually ∼2 km on either side of the trough. The EPR crest over the mapped region shows extensive re-paving by successive volcanic flows as evidenced by scalloped

flow-front margins consistent with eruptions originating from the axis and flowing onto the upper rise flank out to ∼2 km. There are very few faults within ∼2 km of the AST, but we note they are more evident south of the 9° 37′N OSC [*Smith et al.*, 2001]. Most of the faults are low relief (less than ∼10–20 m) based on sonar shadow geometry and ABE micro-bathymetry data, and most trend nearly parallel to the N10°W trend of the EPR axis in this area. There are numerous indications of dendritic lava flow channels emanating from the AST in various sections of the ridge axis principally in the 9° 50′N, 43′–45′N, 37′N, and 26′–29′N areas. Where imaged by deep sea camera, the channels are bounded by lobate flows and floored by smooth-surfaced sheet flows that originate from the AST over areas as great as ∼5 km (along strike in the 9° 26′–29′N area), and coalesce away from

the trough at distances of ~500 m to <1000 m [*Schouten et al.*, 2001, 2002]. Spacing between these areas of inferred sheet flows can be from a few hundred meters to several kilometers.

[7] Fields of ~10–30 m high lava mounds or ridges, several hundred meters wide and up to ~1 km long, occur at distances greater than ~1.5 km from the AST. At times the pillow mounds appear cut by faults and fissures, while in some areas their construction appears to be younger than the tectonic features they overprint.

[8] These observational data suggest that three types of volcanic emplacement have occurred. (1) Eruptions from the AST that primarily result in overlapping/onlapping lobate flows with localized sheet flows. This terrain extends from the axis to ~1–1.5 km from the walls of the AST and give the ridge crest a shingled appearance in plan view. (2) Down-slope flow of lava erupted at or near the AST that has moved through channelized surface flows and lava tubes within the interiors of lobate flows, into the off-axis environment. (3) Off-axis fissure-fed or syntectonic eruptions that form pillow mounds and ridges commonly associated with faulting and tectonism at distances of ~1 km to 4 km off-axis. These magmatic and tectonic processes produce a neovolcanic zone that is up to 4 km wide and results in a "patchwork" of lava flows of potentially different ages [e.g., see *Perfit et al.*, 1994; *Goldstein et al.*, 1993, 1994; *Hooft et al.*, 1996; *Macdonald et al.*, 1996; *Perfit and Chadwick*, 1998; *Kurras et al.*, 2000].

[9] The locations and geological context of the samples used for this study are well constrained (Table 1; Figures 1 and 2). The samples were collected using DSRV Alvin along ~4 km long transects that cross the EPR crest between 9°48′– 52′N. Sample locations were chosen to maximize across-axis spatial coverage and to encompass the range of lava ages and morphologies observed along the dive transects (e.g., they looked young or old, and/or they were located along faults or fissures, or a pillow ridge, etc.). As a result, the samples used for this study provide insights into the temporal and spatial evolution of the EPR crest, and into the volcanic and tectonic processes

responsible for construction of the extrusive oceanic crust.

3. Results

3.1. Major and Trace Elements

[10] Major- and trace-element concentrations are reported in Appendix 1 together with details on analytical methods. All off-axis samples measured in this study are tholeiitic, incompatible trace element depleted, "normal MORB" (N-MORB) with K_2O/TiO_2 < 0.10. Their major-element compositions range from relatively primitive to evolved (molar Mg-number ranging from 64 to 50). More evolved samples have greater concentrations of incompatible trace elements but have incompatible trace element ratios (e.g., La/Yb, Sm/Nd and U/Th) similar to those in basalts with higher Mg-numbers. This group of off-axis samples also shows limited variability in their MgO-normalized Na_2O and FeO contents (Na_8 varies from 2.5 to 2.8, Fe_8 varies from 9.0 to 10.5) and normalized incompatible trace element ratios (e.g., La/Yb, Sm/Nd and U/Th).

[11] With the exception of the most evolved samples, the major-element compositions of the off-axis samples, as a whole (Figure 3, Appendix A), are similar to the compositions reported for the "axial samples" from this region [*Perfit and Chadwick*, 1998; *Sims et al.*, 2002]. The 9°50′N off-axis samples have a slightly larger range of trace element abundances than the axial samples due to higher incompatible and lower compatible trace element concentrations in the most evolved off-axis basalts. However, despite this larger range in trace element abundances (consistent with greater extents of crystal fractionation), all of the off-axis and axial samples show similar patterns on primitive mantle-normalized trace element abundance plots (Figure 4).

3.2. Radiogenic Isotopes: Sr, Nd, Hf and Pb

[12] Sr, Nd, Hf and Pb isotopic compositions for our 9°50′N off-axis samples are reported in Table 2 and shown in Figures 5 through 7. Analytical methods are described in the footnotes to Table 2. With the exception of one highly altered sample (see

Table 1. Sample Locations and Descriptions[a]

Sample	Long. West (Degree, Decimal Minutes)	Lat. North (Degree, Decimal Minutes)	Time of Collection	Depth, m	Description
2737-8	104°18.623	9°50.188	13:27	2525	Pillow from pillow ridge with moderate sediment cover. Aphyric, glassy outer surface is fresh-looking with only slight sediment and Mn-coating
2746-4	104°17.2884	9°48.922	11:37	2515	Young drained out lobe from edge of very collapsed ASC east wall. Appears to be young crust of lobate flow. Very fresh and young-looking, very slight Mn-coating. Slightly plag. phyric with rare crystal clots.
2746-7	104°17.422	9°49.044	12:18	2516	Upper crust of lobate flow in a field of lobate and sheet flows, has slight Mn-and sediment coating, but has thick, fresh glassy top. Mostly aphyric with rare plag microphenocrysts.
2746-9	104°17.679	9°48.971	12:44	2533	Pillow in a hummocky area of small pillows. Sample is from a small, 2–3 m high mound. Very irregularly shaped piece that appears to multiple layers. Surface is hackly to broken probably a reflection of multiple filling and draining of the pillow. Moderate to light sediment and Mn-coating; slightly plag. and ol. phyric.
2746-14	104°18.558	9°49.004	14:10	2658	Massive old flow (~5 m thick); from east-facing (inward) fault scarp that is 10–20 m high with heavy sediment cover on top of scarp; has polygonal jointing, only some thin glass remains on top surface, Heavily coated with MnO. Mostly aphyric, with rare plag. and rarer ol, (see photo)
2759-12	104°18.666	9°49.202	13:08	2650	Pillow recovered from top of inward-facing fault scarp (same scarp as 2746-14); associated with a fissure on top of fault scarp. Moderate Mn-coating. Nearly aphyric with rare plag. microphenocrysts. Not much glass on surface.
2759-14	104°18.581	9°49.203	13:44	2664	Pillow from east of the fault scarp in a field of moderately sedimented pillows (see Side Scan image, Figure 1b). Thick, glass with relatively thin Mn-coating and sediment cover. Slightly plag-phyric.
2768-3	104°15.551	9°49.999	10:43	2675	Pillow basalt bud with extensive sediment cover, part of small flow margin (see photo). In area of short-throw faults and local constructional escarpments. Sample is aphyric and Mn coated.
2768-4	104°15.819	9°50.002	11:24	2611	Pillow with thick Mn coating. From an area of extensive sediment and well-decorated pillow lavas. Sample is aphyric, chalky and partially altered, with up to 1 cm Mn-crust.

Table 1. (continued)[a]

Sample	Long. West (Degree, Decimal Minutes)	Lat. North (Degree, Decimal Minutes)	Time of Collection	Depth, m	Description
2768-6	104°16.363	9°50.002	12:21	2556	Pillow cylinder or tube from a steep constructional escarpment with well-formed pillow cylinders heading down slope, generally heavy sediment cover. Sample is glassy with minimal sediment or Mn coatings.
2768-8	104°16.907	9°50.005	01:37	2530	Lobate flow from an area with curtain-folded sheet flows and collapsed lobate flows; light sediment cover (see photo). Sample is of the glassy lobate crust, relatively fresh-looking, aphyric glass with minimal sediment coating.
2771-1	104°18.655	9°50.02			Lobate flow in moderately sedimented area of low relief. Sample is plag phyric, locally coated with Mn and/or traces of organic remains.
2772-1	104°16.470	9°52.012	08:16	2556	Lobate flow; aphyric with thick glassy margin, moderate sediment and Mn coating.
2772-2	104°16.921	9°52.021	09:08	2555	Lobate flow from collapse area. Sample has thick glassy crust that is plag phyric; Thin Mn coating and minimal sediment (see photo).
2772-3	104°17.238	9°52.014	09:59	2557	Pillow lava bud from base of scarp, moderate sediment cover (see photo). Sample is aphyric with slight Mn coating.

[a] Sample collected using Alvin [*Haymon et al.*, 1993; *Perfit et al.*, 1994; *Fornari et al.*, 1998; *Perfit and Chadwick*, 1998]. Locations are based on transponder navigation in ALVIN. Geological and petrological descriptions summarized from dive transcripts, hand-sample descriptions at sea, and dive films.

2768-8

2768-3

2746-4
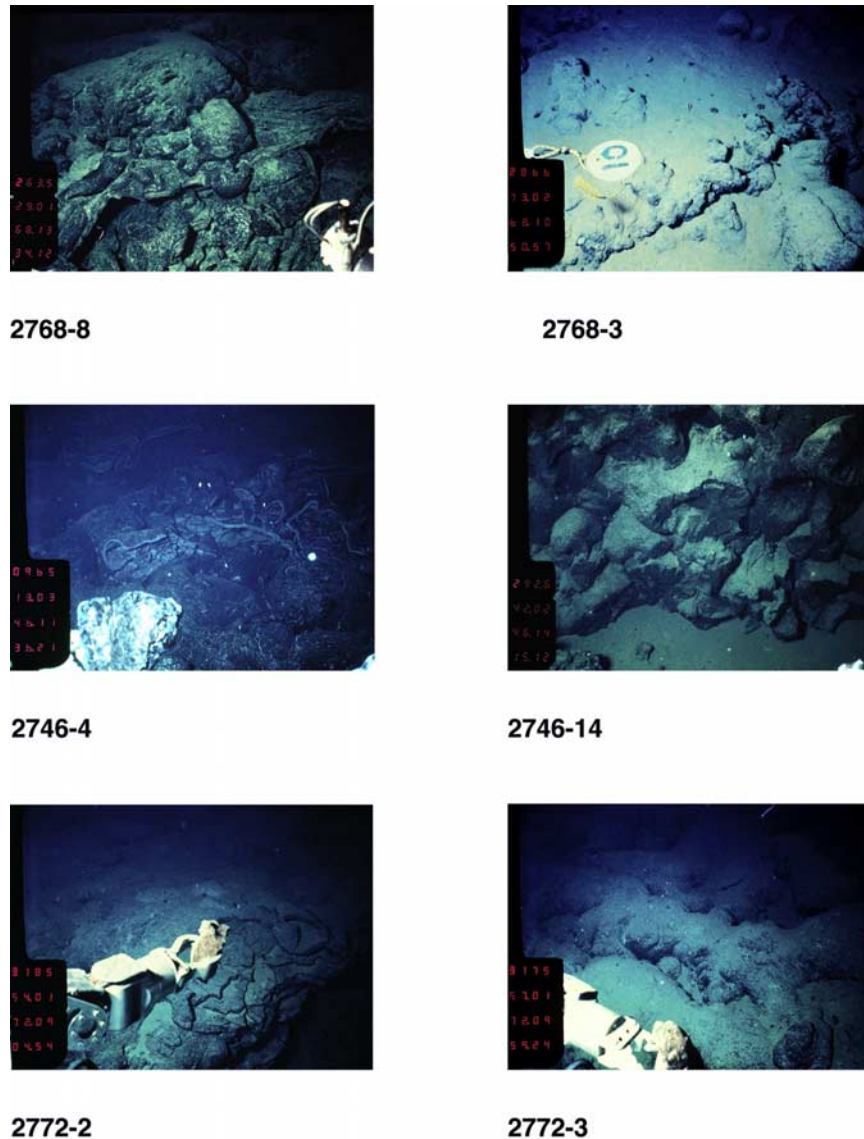

2746-14

2772-2

2772-3

Figure 2. Photos of six of the samples analyzed in this study, taken from Alvin dive tapes. Scale estimates for the six photographic images are: 2768-8 (3×4 m); 2746-4 (4×5 m); 2772-2 (3×4 m); 2768-3 (4×5 m); 2746-14 (2×3 m); 2772-3 (4×5 m). These photos represent the younger (on the left) and older samples (on the right) collected on three different dives (2768; 2746; 2772), and show a distinct contrast in the geologic features that can be related to their age, including sediment cover, Mn oxide coatings, freshness of glass etc. Consistency between these observational features and the ages determined by U-Th-Ra chronology (Table 4) provides validation of the U-series technique.

discussion below), the Sr, Nd, and Hf isotopic compositions exhibit only slight differences (^{87}Sr/^{86}Sr ranges from 0.70244 ± 5 to 0.70254 ± 6; ^{143}Nd/^{144}Nd from 0.512387 ± 10 to 0.512412 ± 9; and ^{176}Hf/^{177}Hf from 0.283157 ± 8 to 0.283194 ± 8). The high-precision ^{208}Pb/^{204}Pb, ^{207}Pb/^{204}Pb, and ^{206}Pb/^{204}Pb data show small but significant variability, whereas the ^{208}Pb/^{206}Pb isotopic ratios

are identical within analytical uncertainty (2.063 ± 1 to 2.065 ± 1).

[13] As a group, the Sr, Nd, Hf and Pb isotopic compositions of the off-axis samples are identical, within analytical uncertainty, to those measured in the 9°50′N EPR axial samples (Figures 5−7) [*Sims et al.*, 2002]. The nearly constant and similar Sr, Nd,
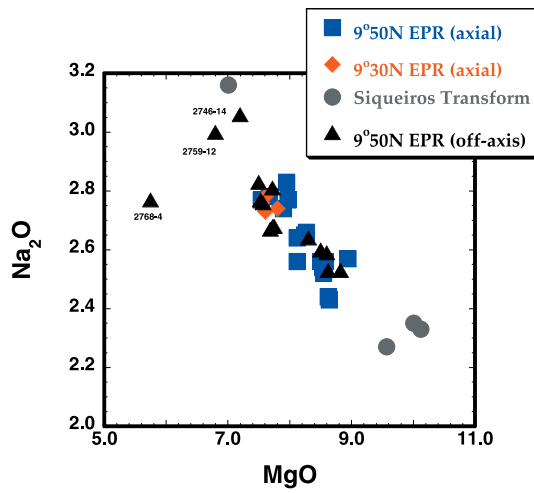
Figure 3. Na$_2$O versus MgO for the 9°50N EPR off-axis samples of this study, the AST lavas from 9°–10°N EPR [*Sims et al.*, 2002], and the Siqueiros picritic basalts and E-type MORB [*Perfit et al.*, 1996]. The axial lavas distinguished as 9°50′N EPR (blue) are from 9°40′N–9°52′N, and those distinguished as 9°30′N EPR (red) come from 9°28′N–9°37′N; this divide is based on a small overlapping spreading center (OSC) at 9°37′N EPR that acts as a hydrothermal and volcanological divide between the northern and southern ridge segments. Note that the altered sample 2768-4 does not lie along the same trend as the other data.

Hf and ^{208}Pb/^{206}Pb isotopic compositions of the axial and off-axis lavas indicate that both sample suites originated from a source that was relatively homogeneous with respect to its time-integrated Rb/Sr, Sm/Nd, Lu/Hf, and Th/U, respectively.

3.3. U-Series Disequilibria Measurements

[14] U, Th, and Ra concentrations and (^{234}U/^{238}U), (^{230}Th/^{232}Th), (^{230}Th/^{238}U) and (^{226}Ra/^{230}Th) for the off-axis 9°50′N samples are reported in Table 3 and shown in Figures 8 and 9. The analytical methods are discussed in the footnotes to Table 3. For several samples, (^{230}Th/^{232}Th) has been measured by both Secondary Ion Mass Spectrometry (SIMS), using the WHOI/NENIMF Cameca IMS 1270 [*Layne and Sims*, 2000], and by Plasma ionization multicollector mass spectrometry (PIMMS), using the Finnigan Neptunes at ThermoFinnigan in Bremen, Germany and at WHOI [*Ball et al.*, 2002]. The reproducibility between the two techniques is within analytical errors (less than 1%). Replicate measurements of (^{238}U/^{232}Th), (^{230}Th/^{232}Th),

(^{230}Th/^{238}U), (^{234}U/^{238}U) and (^{226}Ra/^{230}Th) for MORB sample 2392-9 and rock standards ATHO and TML are consistent (within analytical uncertainties) with previously reported TIMS and SIMS measurements [see *Lundstrom et al.*, 1999; *Sims et al.*, 1995, 1999; *Sims et al.*, 2002].

3.3.1. ^{238}U-^{234}U

[15] For submarine basalts, (^{234}U/^{238}U) activity ratios are a sensitive indicator of alteration, as seawater is significantly enriched in ^{234}U relative to ^{238}U (for seawater (^{234}U/^{238}U) = 1.14 ± 0.03 [*Thurber*, 1962; *Ku et al.*, 1977]). All of the samples analyzed in this study were hand-picked glasses that were mildly leached. Most have (^{234}U/^{238}U) activity ratios = 1.00 (±3 per mil), indicating undetectable post-eruptive alteration (Table 3). However, sample 2768-4, which was one of the most altered and Mn-coated samples in hand-specimen and had partially devitrified glass, has elevated (^{234}U/^{238}U) of 1.009 (±2 per mil), high Cl/K, irregular normalized trace element abundances (e.g., high Ba/Th, negative Ce anomaly), an elevated Sr isotopic composition and slightly lower Hf isotopic compositions (for the mildly leached sample). This sample also has much higher abundances of Th and U (by about a factor of two), lower (^{238}U/^{232}Th), and higher (^{230}Th/^{232}Th) and (^{230}Th/^{238}U) when compared to the other off-axis and axial samples from this region [*Sims et al.*, 2002]. All of this suggests that secondary processes, such as post-eruptive alteration/weathering or the assimilation of altered crust, have significantly changed the chemical and isotopic composition of sample 2768-4. While a strong leach (in warm 6N HCl) seems to diminish this alteration signature (Table 2), such leaching can significantly affect the measured U, Th, and Ra concentrations and resulting U-Th-Ra disequilibria. Because the U-series data for this sample cannot be considered reliable, we do not consider it in our age calculations and subsequent interpretations; however, for completeness, we list its measured major and trace element and isotopic compositions in the data tables.

3.3.2. ^{238}U-^{230}Th-^{226}Ra

[16] All of the off-axis 9°50′N samples examined in this study have (^{230}Th/^{238}U) greater than one,
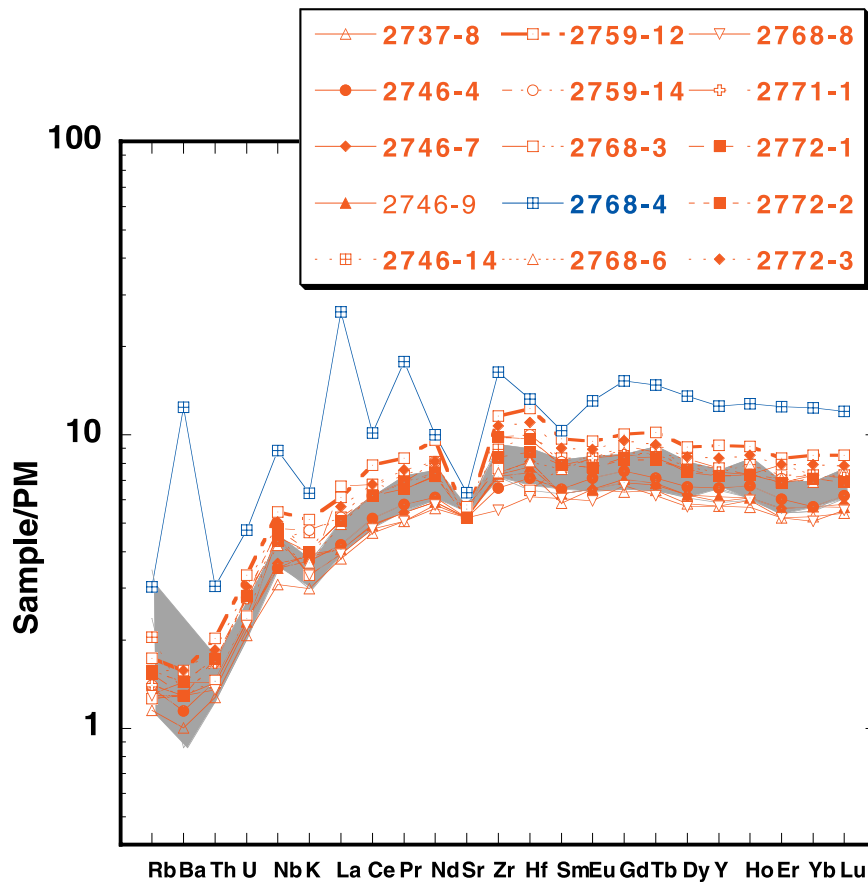
Figure 4. Trace element abundances of off-axis lavas normalized to primitive mantle abundances of *McDonough and Sun* [1995]. Grey field shows the range of normalized abundances for the 9°50′N axial samples. The prominent negative Sr anomalies are a consequence of extensive plagioclase fractionation. Note that if the 9°30′N EPR axial samples, which have similar patterns but higher abundances [*Sims et al.*, 2002], had been included, the axial field would extend beyond the range observed for the 9°50′N off-axis lavas. The pattern of the altered sample (2768-4) is shown in blue and is quite distinct from the other samples.

indicating that the daughter ^{230}Th has been enriched relative to its parent ^{238}U (hereafter (^{230}Th/^{238}U) > 1 is referred to as ^{230}Th excess). Experimentally determined U and Th mineral-melt partition coefficients suggest that ^{230}Th excesses measured in MORB indicate that melting began deep and most likely in the presence of garnet [*Beattie*, 1993; *LaTourrette et al.*, 1993; *Landwehr et al.*, 2001]. For most of the off-axis samples, (^{230}Th/^{232}Th) is correlated with (^{238}U/^{232}Th) (Figure 8), a feature common to the axial samples from 9°50′N EPR [*Sims et al.*, 1995]. There are, however, three samples that lie below this trend and we interpret this to indicate that they are older (see discussion below). Similar to the axial samples, there is a negative correlation between Mg# and the extent of (^{230}Th/^{238}U) disequilibrium in the

off-axis samples. The more primitive samples show the smallest ^{230}Th excesses and the more evolved samples show progressively larger ^{230}Th excesses (Figure 10a).

[17] (^{226}Ra/^{230}Th) is greater than unity in seven of the eleven off-axis samples (Table 3; Figure 9), indicating that daughter ^{226}Ra is enriched relative to its parent ^{230}Th (hereafter (^{226}Ra/^{230}Th) > 1 is referred to as ^{226}Ra excess). The other four samples have ^{226}Ra in equilibrium with ^{230}Th. When compared with the correlation between ^{226}Ra and ^{230}Th excesses of the axial lavas (Figure 9), four of the off-axis samples have large ^{226}Ra excesses similar to the axial samples from this region. The other three samples also have significant ^{226}Ra excesses, but appear to lie on

Table 2. Sr, Nd, Hf and Pb Isotopic Compositions for the 9°50′N EPR Off-Axis Samples[a]

Sample	$^{87}Sr/^{86}Sr$	$^{143}Nd/^{144}Nd$	ε_{Nd}	$^{176}Hf/^{177}Hf$	ε_{Hf}	$^{208}Pb/^{204}Pb$	$^{207}Pb/^{204}Pb$	$^{206}Pb/^{204}Pb$	$^{208}Pb/^{206}Pb$
2737-8	0.70248 ± 5	0.512412 ± 9	11.3	0.283189 ± 8	14.7	37.674	15.467	18.263	2.063
2746-4	0.70247 ± 5	0.512398 ± 12	11.0	0.283190 ± 5	14.8	37.646	15.461	18.250	2.063
2746-7	0.70254 ± 6	0.512396 ± 9	11.0	0.283177 ± 12	14.3				
2746-9	0.70250 ± 4	0.512402 ± 11	11.1	0.283176 ± 10	14.3	37.645	15.454	18.252	2.063
2746-14	0.70248 ± 4	0.512400 ± 10	11.0	0.283178 ± 10	14.4				
2759-12	0.70248 ± 4	0.512409 ± 9	11.2	0.283183 ± 10	14.5				
2759-14	0.70250 ± 3	0.512402 ± 9	11.1	0.283178 ± 8	14.4	37.729	15.498	18.284	2.064
2768-3	0.70248 ± 5	0.512397 ± 11	11.0						
2768-4 (SL)	0.70245 ± 4	0.512400 ± 10	11.0			37.707	15.484	18.267	2.064
2768-4 (LL)	0.70342 ± 12			0.283157 ± 8	13.6				
2768-6	0.70247 ± 4	0.512411 ± 11	11.2	0.283179 ± 11	14.4	37.691	15.476	18.257	2.065
2768-8	0.70244 ± 5	0.512390 ± 12	10.8	0.283175 ± 10	14.3	37.717	15.479	18.273	2.064
2771-1	0.70246 ± 4	0.512410 ± 10	11.2	0.283181 ± 11	14.5	37.662	15.466	18.249	2.064
2772-1	0.70254 ± 6	0.512402 ± 9	11.1	0.283182 ± 10	14.5	37.773	15.503	18.284	2.066
2772-2	0.70252 ± 4	0.512395 ± 11	10.9	0.283176 ± 8	14.3	37.757	15.498	18.278	2.066
2772-3	0.70249 ± 4	0.512387 ± 10	10.8	0.283194 ± 8	14.9	37.754	15.495	18.279	2.065

[a] Glass samples were leached on the ship in either distilled water, 3N HCl or 6N HCl for 15 min, depending on the cruise. In the laboratory samples were hand-picked under a microscope, then ultrasonically leached in sequential treatments of 0.1N HCL plus 2%H_2O_2 (15 min), DI water (twice, each time for 15 min), 0.1N oxalic acid plus 2% H_2O_2, DI water (twice, each time for 15 min), acetone (15 min). Samples were then hand-picked by microscope for a second time and then lightly leached in the clean lab using 0.1N HCL plus 2%H_2O_2 (15 min). All laboratory leaching used ultra pure reagents. For sample 2768-4, which appeared to be highly altered in hand specimen (see text for details) a separate split for the isotopic fraction was further leached with warm 6N HCl until all visible signs of alteration were eliminated; this sample split is designated with the suffix SL (Strong Leach) and is distinguished from the split which was treated as described above designated LL (light leach). Sr isotopes measured at WHOI by TIMS using the VG 354. Uncertainties in measured Sr isotope ratios represent analytical errors ($2\sigma/\sqrt{n}$, where n is the number of measured ratios) reported in the last decimal place. Measured ratios are corrected to NBS987 = 0.710240 measured every fifth sample. External reproducibility is 20–30 ppm based on replicate runs of NBS987. Nd isotopes measured at UC Berkeley by TIMS using the VG 354. Uncertainties in measured Nd isotope ratios are analytical errors ($2\sigma/\sqrt{n}$, where n is the number of measured ratios) reported in the last decimal place. Measured ratios are normalized to $^{146}Nd/^{142}Nd = 0.636151$. Replicate measurement (n = 71) of $^{143}Nd/^{144}Nd$ in BCR-1 (between 10/02/92–4/04/01) gives a value of 0.511843 ± 5. ε_{Nd} values calculated using $(^{143}Nd/^{144}Nd)_{Chur(0)} = 0.511836$, see *DePaolo*, 1988. Hf isotopes measured at ENS Lyon by MC-ICPMS using the VG Plasma 54 [see *Blichert-Toft et al.*, 1997]. Uncertainties in measured Hf isotope ratios are analytical errors ($2\sigma/\sqrt{n}$, where n is the number of measured ratios) reported in the last decimal place. Measured ratios are normalized for mass fractionation to $^{179}Hf/^{177}Hf = 0.7325$. Measurement of $^{176}Hf/^{177}Hf$ in the JMC-475 Hf isotopic standard = 0.28216 ± 1; JMC-475 Hf isotopic standard was run every second sample. ε_{Hf} values calculated with $(^{176}Hf/^{177}Hf)_{Chur(0)} = 0.282772$. Pb isotopes measured at ENS Lyon by MC-ICPMS using the VG Plasma 54. Measured ratios are normalized to both an internal Tl std and then to NBS 981 using the values of *Todt et al.*, 1996. For these measurements every two samples are interspersed with an analyses of NBS 960 for the mass bias correction [see *White et al.*, 2000]. Errors for $^{208}Pb/^{204}Pb$; $^{207}Pb/^{204}Pb$ and $^{206}Pb/^{204}Pb$ are 300–400 ppm (2σ) and for $^{208}Pb/^{206}Pb$ 200–300 ppm (2σ) and are calculated by propagating ($\sqrt{(se^2 + se^2)}$) both the analytical error and the variance of the NBS 960 standards from the instrument fractionation trend observed during the sum of these analyses.

downward vertical trajectories from the axial trend toward ^{230}Th - ^{226}Ra equilibrium.

4. Constraints on Eruption Ages From Measurements of U-Th-Ra Disequilibria
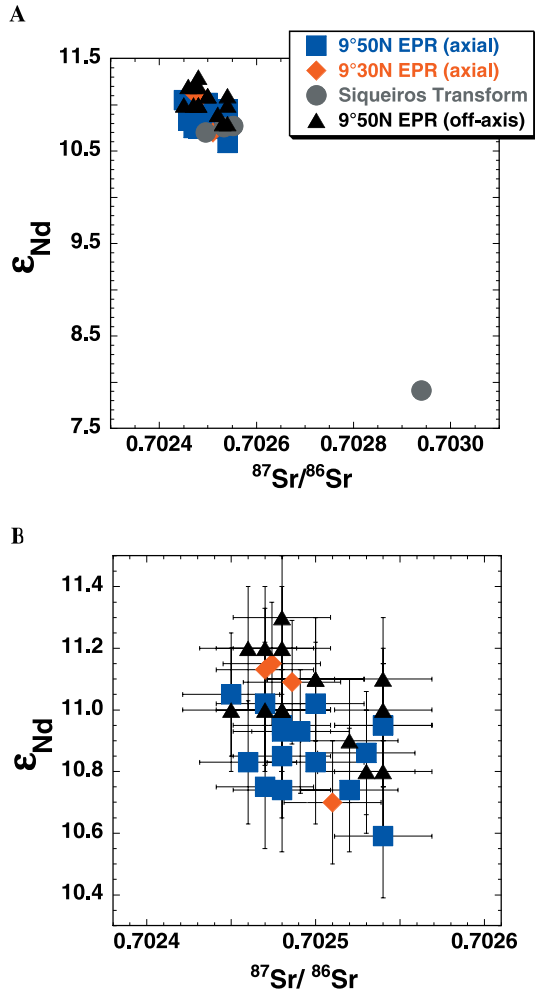
4.1. U-Series Age Constraints

[18] Disequilibrium between a parent/daughter ratio in MORB is generally attributed to chemical fractionation during magmatic processes (e.g., melt generation and transport, crystal fractionation, or magma degassing). If this fractionation ceases after the basalt has erupted (i.e., the system is closed), then the simple presence or absence of radioactive disequilibria can place limits on the time since chemical fractionation (in this case, the eruption age). Because of the large difference in

the half-lives of ^{230}Th (75 ka) and ^{226}Ra (1.6 ka), combined measurement of U-Th and Th-Ra disequilibria enables the dating of MORB across a time range of ca. 10^2–10^6 years.

[19] All thirteen unaltered samples show significant ($^{230}Th/^{238}U$) disequilibria (Table 3), requiring that their eruption ages be less than 300,000 years (Table 4). The large magnitude of these ^{230}Th excesses suggests even younger ages, probably less than the half-life of ^{230}Th (75,000 yrs). This is consistent with the fact that all the samples were collected on crust that is younger than 80 ka, based on spreading rate and their location relative to the AST. Of these thirteen samples, eleven have been measured for ($^{226}Ra/^{230}Th$). Seven of the eleven samples show significant ^{226}Ra excesses. The observation that the ($^{226}Ra/^{230}Th$) is greater than one constrains the ages of these samples to less than

tional to the half-life of the daughter isotope. This decay can be used for dating off-axis MORB [e.g., *Rubin and MacDougall*, 1990; *Goldstein et al.*, 1991, 1993, 1994].

[21] For MORB, U-Th and Th-Ra model ages can be determined from the relationships:

$$T = -\frac{1}{\lambda_{230}} \ln \frac{\left(^{230}Th/^{232}Th\right)_m - \left(^{238}U/^{232}Th\right)_m}{\left(^{230}Th/^{232}Th\right)_o - \left(^{238}U/^{232}Th\right)_m} \quad (1)$$

$$T = -\frac{1}{\lambda_{226}} \ln \frac{\left(^{226}Ra/^{230}Th\right)_m - 1}{\left(^{226}Ra/^{230}Th\right)_o - 1} \quad (2)$$

Figure 5. (a) ε_{Nd} versus $^{87}Sr/^{86}Sr$ for axial 9–10°N and Siqueiros Transform samples [*Sims et al.*, 2002] and 9°50′N off-axis samples measured in this study. Analytical uncertainties are smaller than, or similar to, symbol size. (b) ε_{Nd} versus $^{87}Sr/^{86}Sr$ for axial 9–10°N [*Sims et al.*, 2002] and 9°50′N off-axis samples measured in this study. Error bars represent two sigma analytical uncertainties.

8,000 years. The large magnitude of these ^{226}Ra excesses suggest even younger ages (Table 4). Four of the eleven samples (2746-9, 2746-14, 2759-12, 2768-3) have ($^{226}Ra/^{230}Th$) equal to unity, suggesting their eruption ages are older than 8,000 years. Consequently, the ages of these four samples are constrained to between 8,000 and 300,000 years.
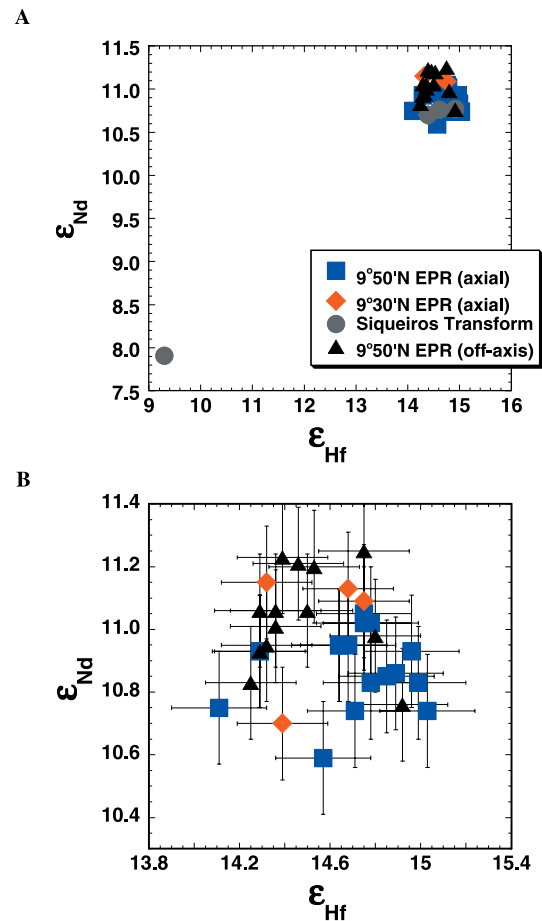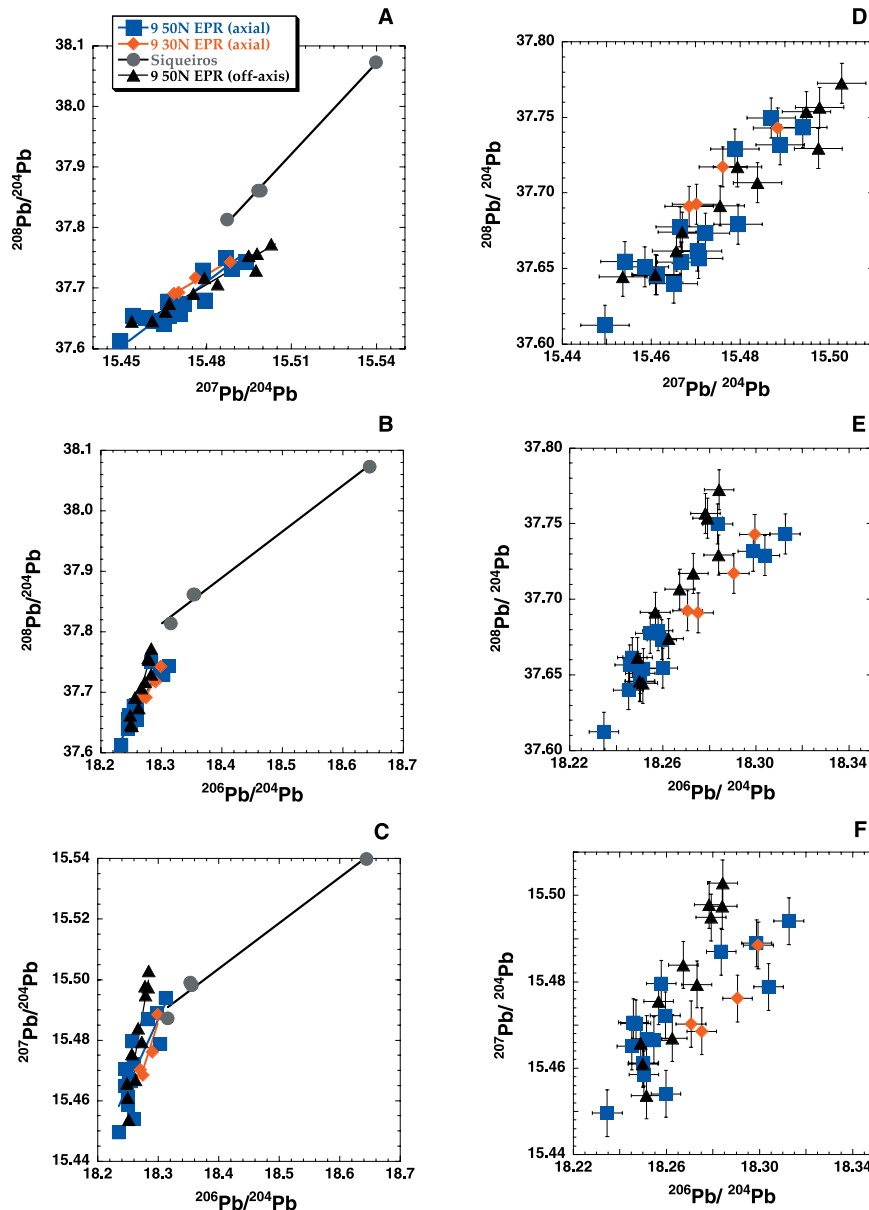
4.2. U-Series "Model" Ages

[20] If after eruption the sample remains a closed system, disequilibria between parent and daughter will decay back to equilibrium at a rate propor-

Figure 6. (a) ε_{Nd} versus ε_{Hf} for axial 9–10°N and Siqueiros Transform samples [*Sims et al.*, 2002] and 9°50′N off-axis samples measured in this study. Analytical uncertainties are smaller than, or similar to, symbol size. (b) ε_{Nd} versus ε_{Hf} for axial 9–10°N [*Sims et al.*, 2002] and 9°50 N off-axis samples measured in this study. Error bars represent two sigma analytical uncertainties.

Figure 7. (a) $^{208}Pb/^{204}Pb$ versus $^{206}Pb/^{204}Pb$, (b) $^{207}Pb/^{204}Pb$ versus $^{206}Pb/^{204}Pb$ and (c) $^{208}Pb/^{204}Pb$ versus $^{207}Pb/^{204}Pb$ for axial 9–10°N and Siqueiros Transform samples [*Sims et al.*, 2002] and 9°50′N off-axis samples measured in this study. (d) $^{208}Pb/^{204}Pb$ versus $^{206}Pb/^{204}Pb$, (e) $^{207}Pb/^{204}Pb$ versus $^{206}Pb/^{204}Pb$ and (f) $^{208}Pb/^{204}Pb$ versus $^{207}Pb/^{204}Pb$ for axial 9–10°N and Siqueiros Transform samples [*Sims et al.*, 2002] and 9°50′N off-axis samples measured in this study. Analytical uncertainties are <400 ppm (2σ) and shown in Figures 7d–7f and similar to symbol size in Figures 7a–7c.

where the subscript (m) represents the sample's measured activity ratio, the subscript (o) its initial activity ratio upon eruption, and λ_{230} and λ_{226} the decay constants for ^{230}Th and ^{226}Ra, respectively. In equation 1, ^{232}Th is used as a stable analog for ^{230}Th [see *Allegre and Condomines*, 1982]. No stable analog exists for ^{226}Ra, hence the different form of equation (2).

[22] In both of these equations, the one additional unknown, besides time, is the sample's initial activity ratio {i.e., $(^{230}Th/^{232}Th)_o$ and $(^{226}Ra/^{230}Th)_o$}. For off-axis MORB, U-series ages can be determined by estimating this initial activity ratio from data for young axial basalts and comparing this with the sample's measured activity ratio. For this approach to be valid, it must be dem-

Table 3. $(^{230}\text{Th}/^{232}\text{Th})$, $(^{230}\text{Th}/^{238}\text{U})$, $(^{226}\text{Ra}/^{230}\text{Th})$, $(^{234}\text{U}/^{238}\text{U})$, and U, Th and Ra Concentrations Measured by SIMS, PIMMS and Single-Collector ICPMS[d,e,f]

Sample	[Th] ug/g	[U] ug/g	Th/U	$(^{238}\text{U}/^{232}\text{Th})$	$(^{230}\text{Th}/^{232}\text{Th})$	$(^{230}\text{Th}/^{238}\text{U})$	[^{226}Ra] fg/g	$(^{226}\text{Ra}/^{230}\text{Th})$	$(^{234}\text{U}/^{238}\text{U})$
2737-8 (1)	0.1085[a]	0.0436[a]	2.488	1.219	1.375[a]	1.127			1.002[b]
2737-8 (2)					1.375[b]	1.127			
2737-8 *avg*					*1.375*	*1.127*			
2746-4	0.1229[a]	0.0496[a]	2.479	1.224	1.390[a]	1.135	50.89	2.67	1.003[a]
2746-7	0.1214[a]	0.0486[a]	2.498	1.215	1.376[a]	1.133	49.45	2.66	
2746-9 (1)	0.1212[a]	0.0483[a]	2.507	1.210	1.351[a]	1.116	18.40	1.01	1.002[a]
2746-9 (2)					1.361[b]	1.124			
2746-9 *avg*					*1.356*	*1.120*			
2746-14	0.1432[a]	0.0587[a]	2.441	1.243	1.351[a]	1.087	21.44	0.99	1.001[b]
2759-12	0.1717[a]	0.0699[a]	2.458	1.234	1.383[a]	1.120	26.25	0.99	
2759-14	0.1433[a]	0.0587[a]	2.441	1.243	1.398[a]	1.125	50.65	2.27	
2768-3	0.1239[a]	0.0507[a]	2.445	1.241	1.322[a]	1.065	18.25	1.00	1.002[b]
2768-4	0.2594[a]	0.0994[a]	2.608	1.163	1.402[a]	1.205			1.009[b]
2768-6 (1)	0.1466[a]	0.0588[a]	2.494	1.216	1.380[a]	1.134			1.001[a]
2768-6 (2)					1.383[a]	1.137			
2768-6 (avg)					1.381	1.136			
2768-8 (1)	0.1148[a]	0.0470[a]	2.443	1.242	1.386[a]	1.116			
2768-8 (2)					1.384[b]	1.114			1.003[b]
2768-8 (avg)					1.385	1.115			
2771-1	0.1421[a]	0.0582[a]	2.442	1.242	1.393[a]	1.122	49.00	2.23	1.003[b]
2772-1 (1)	0.1466[a]	0.0595[a]	2.461	1.233	1.420[a]	1.152	59.65	2.58	1.002
2772-1 (2)					1.423[b]	1.155			
2772-1 (avg)					1.422	1.153			
2772-2	0.1466[a]	0.0594[a]	2.466	1.230	1.412[a]	1.148	61.65	2.68	
2772-3 (1)	0.1572[a]	0.0637[a]	2.468	1.229	1.385[a]	1.126	50.10	2.07	1.002[a]
2772-3 (2)					1.380[b]	1.122			1.003[b]
2772-3 (avg)					1.382	1.124			
AThO					1.013[b]				1.002[b]
AThO					1.014[a]				
TML 1LANL	30.26[a]	10.80[a]	2.801	1.083	1.086[c]	1.003	3,623	0.991	1.004[a]
TML-2 LANL	30.49[a]	10.87[a]	2.804	1.082	1.072[c]	0.991	3,635	0.999	
TML 1WHOI	29.45[b]	10.543[b]	2.793	1.086	1.084[a]	0.997			1.004[b]
TML 2 WHOI	29.44[b]	10.517[b]	2.799	1.084	1.084[a]	0.999			1.002[b]
TML 3 WHOI	30.17[b]	10.695[b]	2.821	1.076	1.082[a]	1.006			1.005[b]
TML 4 WHOI					1.069[b]				
TML 5 WHOI					1.072[b]				

[a] Duplicate measurements represent separate glass splits; glass samples were leached on the ship in either distilled water or 6N HCl for 15 min, depending on the cruise. In the laboratory the samples were hand-picked under a microscope, then ultrasonically leached in sequential treatments of 0.1N HCL plus 2%H_2O_2 (15 min), DI water (twice, each time for 15 min), 0.1N oxalic acid plus 2% H_2O_2, DI water (twice, each time for 15 min), acetone (15 min). Samples were then hand-picked by microscope for a second time and then lightly leached in the clean lab in 0.1N HCL plus 2%H_2O_2 (15 min) using ultra pure reagents. Sample splits (>1 g) were then dissolved, aliquoted, spiked and then U-Th-Pa and Ra were separated using chemical techniques outlined in *Goldstein et al.*, 1989; *Volpe et al.*, 1991; *Cohen and O'Nions*, 1991; *Chaubaux et al.*, 1994; and *Layne and Sims*, 2000. Note that measurements of TML, leached under similar conditions, show that this leaching procedure does not alter the samples U and Th concentrations.

[b] [U], [Th], measured by both a) ID-TIMS at LANL and b) ID-ICPMS at WHOI; measurement errors for [U], [Th] ≤0.8% (2σ) for ID-TIMS and ≤1.0% for ID-ICPMS.

[c] ( ) denotes activity $\lambda_{238} = 1.551 \times 10^{-10}$ yr^{-1};, $\lambda_{232} = 4.948 \times 10^{-11}$ yr^{-1} errors (2σ) range from 0.4%–1.0% and do not include uncertainties in λ_{238} (0.07%) or λ_{232} (0.5%).

[d] Th isotopic compositions measured by a) SIMS at WHOI [*Layne and Sims*, 2000]; B) PIMMS at Finnigan MAT in Bremen and WHOI using the ThermoFinnigan Neptune [*Ball et al.*, 2002] c HAS TIMS at LANL [*Goldstein et al.*, 1989; *Sims et al.*, 1995, 1999]; activity ratios calculated using $\lambda_{230} = 9.195 \times 10^{-6}$ yr^{-1} and $\lambda_{232} = 4.948 \times 10^{-11}$ yr^{-1}; errors (2σ) range from: 0.4%–1% for both techniques and do not include uncertainties in λ_{230} (0.4%) or λ_{232} (0.5%).

[e] (^{226}Ra) measured by ID-ICPMS at WHOI using the ThermoFinnigan Element; $\lambda_{226} = 4.331 \times 10^{-4}$ yr^{-1}, ;measurement errors (2σ range from 0.6%–1.7% and do not include uncertainties in λ_{226} (0.4%) or λ_{230}. For all samples accuracy is limited by uncertainties (2σ; 1.5%) on the NBS ^{226}Ra standard used to calibrate the ^{228}Ra spike.

[f] $(^{234}\text{U}/^{238}\text{U})$ measured by a) TIMS at LANL and by b) ICPMS at WHOI. $\lambda_{234} = 2.823 \times 10^{-6}$ yr^{-1}, errors (2σ) < 1.0%; for these samples $(^{234}\text{U}/^{238}\text{U}) = 1$ within error, using an equilibrium ^{234}U/^{238}U of 54.95 ppm. For ICPMS NBS 960 was run between each sample to determine mass bias.
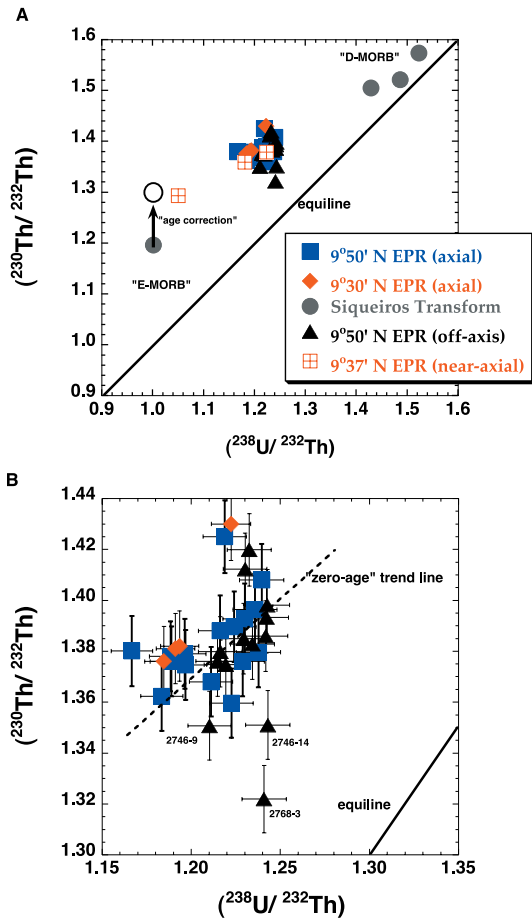
Figure 8. (a) $(^{238}U/^{232}Th)$ versus $(^{230}Th/^{232}Th)$ for 9°50′N off-axis samples compared to the 9–10°N EPR axial samples [*Sims et al.*, 2002], and the Siqueiros Transform samples [*Lundstrom et al.*, 1999; *Sims et al.*, 2002] for which Sr, Nd, Hf and Pb isotopes have been measured. Note that the age of Siqueiros E-type sample (2390-1) is thought to be significant relative to the half-life of ^{230}Th and has been age corrected [see *Lundstrom et al.*, 1999]. Also shown are the near axial basalts from 9°37′N EPR [Goldstein et al., 1992]. (b) U/Th versus $^{230}Th/^{232}Th$ for the 9°50′N off-axis samples compared to the 9–10°N EPR axial samples [*Sims et al.*, 2002]. Errors represent two sigma analytical uncertainties. Dashed line represents the zero-age axial trend used for calculating "trend line" ages. For most of the off-axis samples $(^{230}Th/^{232}Th)$ and $(^{238}U/^{232}Th)$ are similar to the axial samples from 9°50′N EPR; the three samples which lie below the range of axial values are interpreted to be older (see text for details).

onstrated that both the axial and off-axis lavas were: (1) derived from the same time-averaged source (as indicated by their Sr, Nd, Hf and Pb isotopic compositions), and (2) produced by

similar petrogenetic processes (i.e., similar melt fractions, depths of melting, transport mechanisms, extents of magma differentiation, and magma transport and storage times).
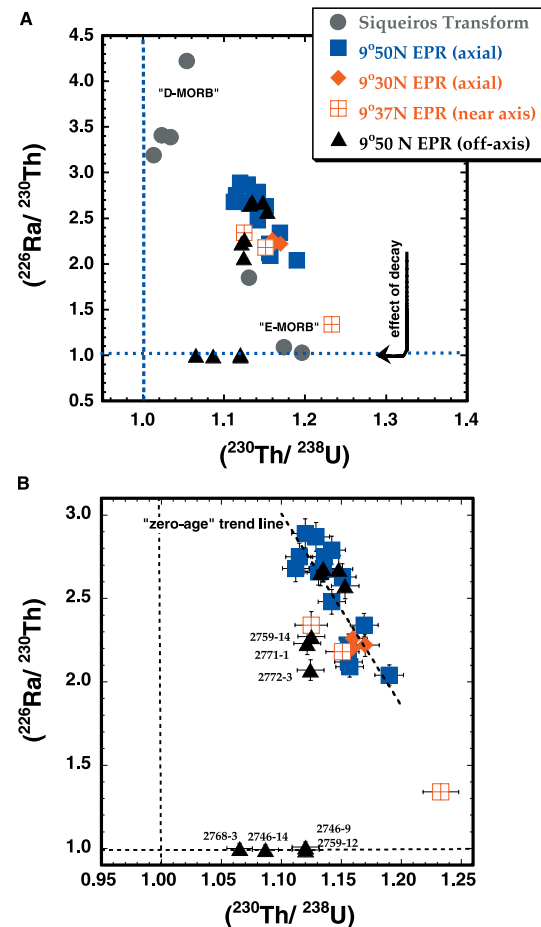
Figure 9. (a) $(^{230}Th/^{238}U)$ versus $(^{226}Ra/^{230}Th)$ for the 9°50′N EPR off-axis samples from this study compared with the 9–10°N EPR axial samples [*Sims et al.*, 2002], three "near axis" 9°30N EPR samples, including one E-type from close to the 9°37′N DEVAL [*Batiza and Niu*, 1992; *Volpe and Goldstein*, 1993] and the Siqueiros transform samples [*Lundstrom et al.*, 1999]. (b) $^{230}Th/^{238}U$ versus. $^{226}Ra/^{230}Th$ for 9°50′N EPR off-axis samples compared with the 9°50′N EPR axial samples [*Sims et al.*, 2002]. Error bars represent two sigma analytical uncertainties. Because of the significant difference in the half-lives of ^{226}Ra and ^{230}Th, $(^{226}Ra/^{230}Th)$ decays back to equilibrium before $(^{230}Th/^{238}U)$ (note decay curve on plot). The correlation observed among the zero-age samples (shown by dashed line) is used as the trend line from which Th-Ra ages are calculated (see text for details). Note that several off-axis samples have $(^{226}Ra/^{230}Th)$ in equilibrium, indicating that their ages are older (>8 ka) than can be determined through ^{230}Th-^{226}Ra disequilibria.
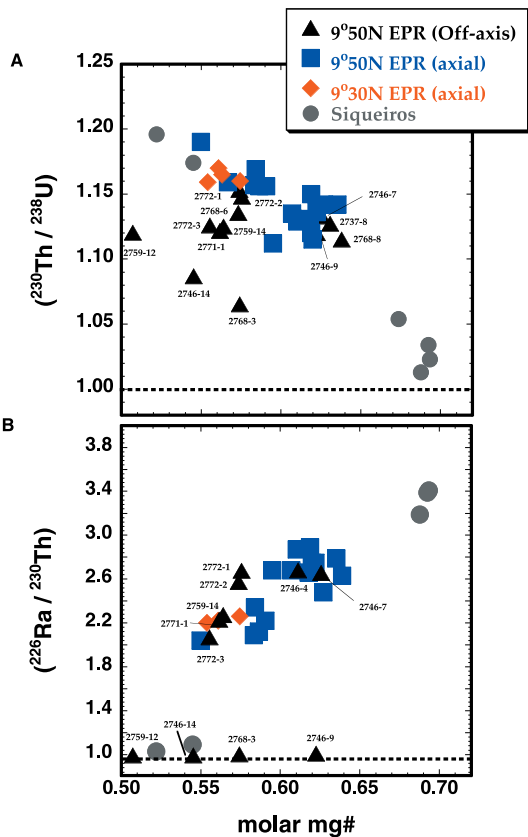
Figure 10. (a) ^{230}Th excess versus Mg# (molar Mg/(Mg + Fe); Fe based on FeO = 0.9 × FeO total)) for the 9°50′N EPR off-axis samples compared with the 9–10°N axial and Siqueiros Transform samples. (b) ^{226}Ra excess versus Mg# for the 9°50′N EPR off-axis samples compared with the 9–10°N axial and Siqueiros Transform samples. For the 9–10°N EPR axial lavas (^{230}Th/^{238}U) and (^{226}Ra/^{230}Th) are correlated with molar Mg#, which is attributed to the mixing of polybaric melts (see *Sims et al.* [2002] for details). Many of the off-axis lavas are similarly correlated, further confirming this functional relationship. Several samples that lie below these correlations have significant U-Th and Th-Ra ages. If the residence times of the young evolved off-axis pillow ridge lavas were significantly different from those of the axial lavas, relative to the half-life of ^{226}Ra, then it is likely that these lavas would lie below the (^{226}Ra/^{230}Th)-Mg# correlation. The observation that the young off-axis samples tend to lie slightly above the (^{226}Ra/^{230}Th)-Mg# correlation, but slightly below the (^{230}Th/^{238}U)-Mg# correlation, suggests that these lavas have been shifted to lower Mg#. If so, one could infer that they had experienced different cooling histories, but the timescale of differentiation is short compared to the half-life of ^{226}Ra.

[23] To calculate U-series model ages for the 9°50′N EPR off-axis samples, initial activity ratios are estimated from young basalts (some erupted in 1991–92; see *Rubin et al.* [1994]), collected exclusively within the AST between 9°48′ and 9°52′N, for which major- and trace element compositions, U-Th-Ra and U-Pa disequilibria and Sr, Nd, Hf, and Pb isotopic compositions have been determined [*Sims et al.*, 2002]. The Sr, Nd, Hf and ^{208}Pb/^{206}Pb isotope compositions in both the axial and off-axis lavas are identical (within analytical uncertainty) indicating that over the length scale of melting, their mantle source was homogenous with respect to its time-averaged parent/daughter ratios (Rb/Sr, Sm/Nd, Lu/Hf and U/Th). However, the young axial lavas from this region show significant variability in U/Th, ^{230}Th/^{232}Th, (^{230}Th/^{238}U) and (^{226}Ra/^{230}Th) (Figures 8 and 9), which we attribute to variations in the degree and depth of melting and the effects of progressive source depletion [*Sims et al.*, 2002]. While this variability has been critical for the interpretation of melting beneath this region of the EPR [*Sims et al.*, 2002], it adds uncertainty when using the axial lavas as a proxy for the off-axis lavas' initial (^{230}Th/^{232}Th) and (^{226}Ra/^{230}Th), and this uncertainty must be taken into account in the U-Th and Th-Ra age calculations.

4.2.1. U-Th Model Ages

[24] Using a statistical interpretation to account for the observed variability among the young axial lavas, we observe that ten of the off-axis samples' (^{230}Th/^{232}Th) are within the range observed for the axial samples (1.362 to 1.425), while the other three samples (2746-9, 2746-14, 2768-3) have lower (^{230}Th/^{232}Th). However, when analytical errors are considered, only sample 2768-3 is significantly different. While using the lowest value of (^{230}Th/^{232}Th) in axial lavas as a proxy for the off-axis lavas' initial activity ratio provides an estimate of minimum age, using the axial lavas upper limit for the initial value provides an estimate of maximum age (Table 4). Most of the off-axis lavas have (^{230}Th/^{232}Th) higher than the axial lavas' lower limit of 1.36, and, therefore, these samples' calculated minimum ages are zero. For samples 2746-9, 2746-14, 2768-3, (^{230}Th/^{232}Th) is smaller

Table 4. Spreading Rate Ages, U-Th and Th-Ra Age Limits and U-Th and Th-Ra Model Ages (See Text for Explanation of Age Calculations)[a]

Sample	Distance From AST, km	Age Based on Spreading Rate, ka	U-Th-Ra Age Constraints, ka	U-Th Minimum Age, ka	U-Th Maximum Age, ka	U-Th Trend Line Age, ka	Th-Ra Minimum Age, ka	Th-Ra Maximum Age, ka	Th-Ra Trend Line Age, ka
2737-8	1.85 W	33.64	<300	0	33 ± 20	0	NM	NM	NM
2746-4	0.02 E	0.28	<8	0	24 ± 19	0	0	0.3 ± 0.1	0
2746-7	0.26 W	4.79	<8	0	31 ± 19	0	0	0.3 ± 0.1	0
2746-9	0.74 W	13.42	8 to 300	0	45 ± 21	15 ± 16	>8	>8	>8
2746-14	2.36 W	42.98	8 to 300	0	60 ± 28	38 ± 24	>8	>8	>8
2759-12	2.56 W	46.64	8 to 300	0	30 ± 21	0	>8	>8	>8
2759-14	2.41 W	43.75	<8	0	20 ± 19	0	0	0.9 ± 0.1	0.7 ± 0.2
2768-3	3.75 E	68.26	8 to 300	42 ± 37	92 ± 35	69 ± 30	>8	>8	>8
2768-6	2.25 E	40.92	<300	0	28 ± 19	0	NM	NM	NM
2768-8	1.24 E	22.63	<300	0	30 ± 21	0	NM	NM	NM
2771-1	1.99 W	36.16	<8	0	24 ± 20	0	0	1.0 ± 0.1	0.8 ± 0.2
2772-1	2.28 E	41.37	<8	0	5 ± 16	0	0	0.4 ± 0.1	0
2772-2	1.44 E	26.21	<8	0	10 ± 17	0	0	0.3 ± 0.1	0
2772-3	0.86 E	15.55	<8	0	30 ± 20	0	0	1.3 ± 0.1	1.1 ± 0.2

[a] AST location determined by *Fornari et al.* [1998]. Spreading determined assuming a constant spreading rate of 5.5 cm/yr half-rate. Age constraints based upon absence of presence of $^{230}Th/^{238}U$ or $^{226}Ra/^{230}Th$ disequilibria and the half-lives of ^{226}Ra and ^{230}Th; see text for details. U-Th minimum and maximum ages calculated using the range of $(^{230}Th/^{232}Th)$ from the 9°50N EPR AST samples (low value: 1.362; high value: 1.425) from *Sims et al.* [2002]; maximum and minimum ages are estimates and assume that the measured range of $(^{230}Th/^{232}Th)$ in the axial samples represents the entire possible range (see text for details). Negative minimum ages are reported as zero years. Errors incorporate analytical uncertainties in $(^{238}U/^{232}Th)$ and $(^{230}Th/^{232}Th)$ of the off-axis samples and $(^{230}Th/^{232}Th)$ of the "end-member" axial samples. U-Th "trend line" ages calculated using "zero-age" trend defined by the 9°50N EPR AST samples on the U-Th isochron plot (see Figure 8). Off-axis samples indistinguishable from the 9°50N EPR AST samples are defined as zero-age. For samples that lie below this "zero-age" trend, their "initial" $(^{230}Th/^{232}Th)$ is inferred by their measured $(^{238}U/^{232}Th)$. Errors incorporate analytical uncertainties in $(^{238}U/^{232}Th)$ and $(^{230}Th/^{232}Th)$ of the off-axis samples and the range of $(^{230}Th/^{232}Th)$ about the zero-age axial trend. Th-Ra minimum and maximum ages calculated using the range of $(^{226}Ra/^{230}Th)$ determined from 9°50N EPR AST samples (2.01 to 2.89) from *Sims et al.* [2002]; maximum and minimum ages are estimates and assume that the measured range of $(^{226}Ra/^{230}Th)$ in the axial samples represents the entire possible range (see text for details). Negative minimum ages are reported as zero years. Samples with ages older than 8 ka have $(^{226}Ra/^{230}Th)$ = 1. Errors incorporate analytical uncertainties in $(^{226}Ra/^{230}Th)$ of both the off-axis samples and the "end-member" axial samples. Th-Ra "trend-line" ages calculated using "zero-age" trend defined by the 9°50N EPR ASCT samples on $(^{226}Ra/^{230}Th)$versus$(^{230}Th/^{238}U)$ (see Figure 9). Off-axis samples indistinguishable from the 9°50N EPR AST samples are defined as zero-age. For samples that lie below this "zero-age" trend, their "initial" $(^{226}Ra/^{230}Th)$ is inferred from their measured $(^{230}Th/^{238}U)$. Samples with ages older than 8 ka have $(^{226}Ra/^{230Th})$ = 1. Errors incorporate analytical uncertainties in $(^{226}Ra/^{230}Th)$ of the off-axis samples and the range of $(^{226}Ra/^{230}Th)$ about the "zero-age" axial trend.

than the axial lavas' lower limit; however, when analytical uncertainties are considered, only 2768-3 is significantly different having a minimum age of 43 ± 35 ka. When calculating "maximum ages", only two of the off-axis samples (2772-1; 2759-14) have maximum ages that are significantly younger than their calculated spreading rate ages, suggesting that these samples were emplaced off-axis. All other off-axis samples have maximum ages that are similar to or older than their calculated spreading rate ages, indicating that they could have originated on or close to the axis. When the minimum and maximum ages are considered in combination, most of these samples have U-Th ages that range from zero years, which would indicate that the sample was emplaced/erupted in its current location, to having maximum ages similar to the inferred spreading rate age, which would indicate that the sample was originally erupted on axis and

has aged proportionally to the spreading rate (see also Figure 11a). In the absence of additional constraints, the large variation in $(^{230}Th/^{232}Th)$ and $(^{230}Th/^{238}U)$ among the axial samples clearly limits the resolution of the above-determined U-Th ages.

[25] A more robust way to estimate the initial $(^{230}Th/^{232}Th)$ and $(^{230}Th/^{238}U)$ of off-axis lavas is to take advantage of the observation that the U-series isotopes of the "zero age" 9°–10°N EPR axial lavas are correlated, both among themselves {e.g., $(^{230}Th/^{232}Th)$ versus $(^{238}U/^{232}Th)$ and $(^{230}Th/^{238}U)$ versus $(^{226}Ra/^{230}Th)$}, and with other chemical indices {e.g., $(^{230}Th/^{238}U)$ versus Mg#} [see *Sims et al.*, 2002]. If it can be shown that young off-axis lavas exhibit similar correlations, then the ages of lavas that deviate from these correlations can be determined explicitly by pro-
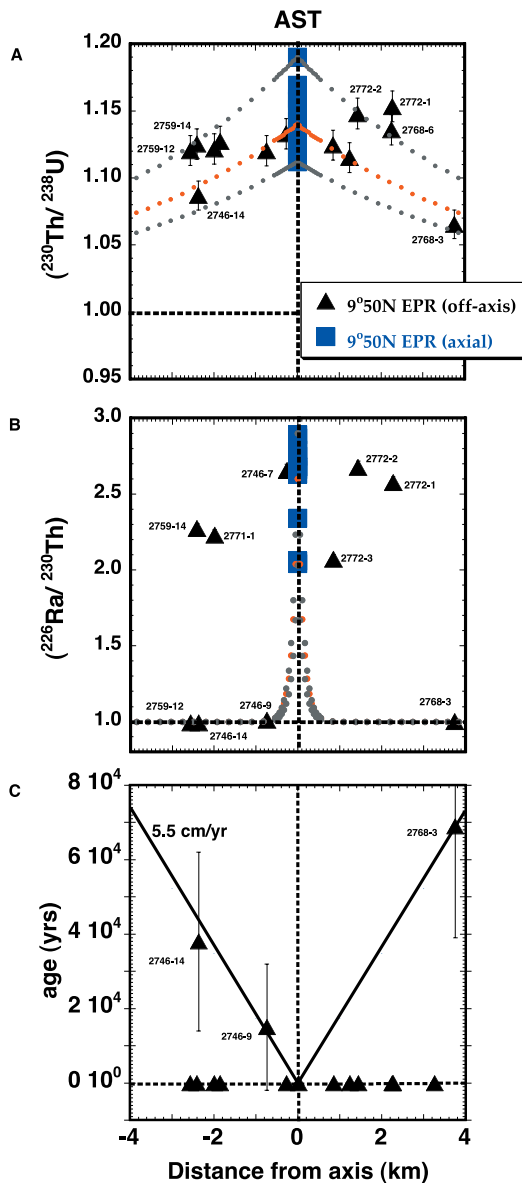
Figure 11. (a) 9°50′N EPR samples $(^{230}Th/^{238}U)$ versus their location, relative to the AST. Decay curves show how $(^{230}Th/^{238}U)$ decreases as a function of distance from the AST. Initial values for decay curves come from the average (1.385 ± 0.02), shown in red, and high (1.425) and low (1.362) values of $(^{230}Th/^{238}U)$ for the 9°50′N EPR axial samples reported in *Sims et al.* [2002]. (b) 9°50′N EPR samples $(^{226}Ra/^{230}Th)$ versus their location relative to the AST. Decay curves show how $(^{226}Ra/^{230}Th)$ decreases as a function of distance from the AST. The initial values for these decay curves come from the average (2.5 ± 0.3), shown in red, and high (2.89) and low (2.01) values of $(^{226}Ra/^{230}Th)$ for the 9°50′N EPR axial samples taken from *Sims et al.* [2002]. (c) U-Th and Th-Ra trend-line ages for the 9°50′N off-axis samples compared with ages calculated from spreading rate (5.5 cm/yr), as determined from paleomagnetic data [*Carbotte and Macdonald*, 1992].

jection to the zero-age trend. We have shown previously that the 9–10°N EPR axial lavas' $(^{230}Th/^{232}Th)$ activity ratios vary as a function of $(^{238}U/^{232}Th)$ (Figure 8). This correlation, which is defined as the "zero-age axial trend", can be used to determine U-Th model ages of the 9°50′N EPR off-axis lavas. All but three of the off-axis samples (2746-9, 2746-14 and 2768-3) have $(^{230}Th/^{232}Th)$ and $(^{238}U/^{232}Th)$ that lie within the zero-age trend, and when analytical errors are considered, only two of these samples (2768-3; 2746-14) are significantly different. Because on a plot of $(^{230}Th/^{232}Th)$ versus $(^{238}U/^{232}Th)$, ^{230}Th decay occurs along vertical vectors (Figure 8b), the "initial" $(^{230}Th/^{232}Th)$ of these samples can be inferred from their measured $(^{238}U/^{232}Th)$. The difference between a sample's measured and projected "initial" $(^{230}Th/^{232}Th)$ is then used to calculate its age. Calculated U-Th ages for samples 2746-9, 2746-14, and 2768-3 are 15 ± 16 ka, 38 ± 24 ka and 69 ± 30 ka, respectively (Table 4).

4.2.2. Th-Ra Model Ages

[26] Four samples (2768-3, 2746-14, 2759-12, 2746-9) have $(^{226}Ra/^{230}Th)$ equal to unity; the Th-Ra ages of these samples therefore cannot be determined, except to say that they are older than 8 ka (or were erupted with ^{226}Ra in equilibrium with ^{230}Th, which is highly unlikely). The other seven off-axis samples have $(^{226}Ra/^{230}Th)$ greater than one. The $(^{226}Ra/^{230}Th)$ of these samples are within the range observed among the 9°50′N axial samples (2.01 to 2.89); calculated minimum ages are "zero" years for all samples, and calculated maximum ages range from 0.3 ± 0.1 ka (2746-4, 2746-7, 2772-2) to 1.3 ± 0.1 ka (2772-3) (Table 4).

[27] A more explicit way to determine Th-Ra ages for the off-axis samples is to use the negative correlation between $(^{226}Ra/^{230}Th)$ and $(^{230}Th/^{238}U)$ observed among the 9°–10°N EPR axial samples (Figure 9). The half-life of ^{226}Ra is very short compared to the half-life of ^{230}Th; for off-axis samples, which do not lie along this correlation, the initial $(^{226}Ra/^{230}Th)$ can be determined by projection from the $(^{230}Th/^{238}U)$. Four samples (2746-4, 2746-7, 2772-1, 2772-2) lie along the zero age axial trend (Figure 9b) and therefore have

"zero" Th-Ra ages relative to this trend line. Three samples (2759-14, 2771-1, 2772-3) have significant ^{226}Ra excesses, but lie somewhat below the zero-age trend; calculated Th-Ra "trend line" ages for these samples are 0.7 ± 0.2 ka, 0.8 ± 0.2 ka and 1.1 ± 0.2 ka, respectively (Table 4). Th-Ra ages for four samples (2768-3, 2746-14, 2759-12, 2746-9) with (^{226}Ra/^{230}Th) equal to unity are greater than 8 ka.

[28] The U-Th and Th-Ra model ages for the 9°50′N EPR off-axis samples are concordant. Samples with large ^{226}Ra excesses have "zero" U-Th model ages, whereas samples with significant U-Th ages have (^{226}Ra/^{230}Th) in equilibrium. All samples with (^{226}Ra/^{230}Th) greater than one are much younger than would be predicted by their spreading rate ages (Table 4); these young ages therefore require that these samples were emplaced off-axis as either flows or eruptions.

4.3. Influence of Magma Chamber Residence Times on Calculated U-Series Ages

[29] In this study we assume that the U-Th-Ra disequilibria are produced by melt generation and magma transport processes. Prior work on the axial samples from 9°–10°N EPR [Sims et al., 2002; Jull et al., 2003], and numerous other related studies [e.g., McKenzie, 1985; Williams and Gill, 1989; Spiegelman and Elliott, 1993; Lundstrom et al., 1995, 1999, 2000] have shown that U-Th-Ra disequilibria in MORB are best explained by melt generation and magma transport processes. Recently it has been proposed that addition of ^{226}Ra from plagioclase (which has a high Ra/Th ratio) either through assimilation or steady-state melt/plagioclase interaction during magma storage could be responsible for the observed Th-Ra disequilibiria in MORB [Saal et al., 2002]. However, recent measurements of ^{226}Ra-^{230}Th in plagioclase and glass from the N. Gorda Ridge 1996 flow [Cooper et al., 2003] limit the extent to which plagioclase could modify ^{226}Ra-^{230}Th disequilibria during storage in a crustal reservoir. The extremely low Th concentrations in the plagioclase (3.3 ± 1.7 ng/g) requires any assimilated plagioclase to be very young (as ^{226}Ra incorporated during crystal-

lization will be unsupported and rapidly decay to equilibrium with the low ^{230}Th) or that the ^{226}Ra concentration in plagioclase is "maintained" by diffusive exchange with a mineral that has a high Th concentration (e.g., pyroxene). The low concentrations of ^{226}Ra measured in the plagioclase (3.4 ± 0.6 fg/g) are even more problematic. While the (^{226}Ra)/(^{230}Th) measured in plagioclase from the N. Gorda Ridge sample is much higher (7.3) than that in the glass (2.4), the absolute concentration of Ra in plagioclase is more than a factor of 10 lower than that in the coexisting glass. Addition of 50% plagioclase by assimilation to a liquid with a composition like that of the host glass would raise (^{226}Ra)/(^{230}Th) in the liquid to only ~2.5 and significantly change the bulk composition of the liquid (which is not evident in the 9–10°N EPR major and trace element data). If instead steady-state melt/plagioclase diffusive exchange were the operative process, then the ratio of cumulate/melt would have to be quite large, requiring an excessive amount of cumulate to produce the observed 7 km thick oceanic crust. Such a process would also have to be systematic enough to generate the observed correlation between ^{230}Th and ^{226}Ra excesses. In either case, melting or cumulate-melt interaction, the U-series "clocks" start when the melt is no longer in equilibrium with the matrix.

[30] When magma is stored in the crust for a significant period of time prior to eruption, U-Th and Th-Ra disequilibria can decay toward their equilibrium values. We are using the axial lavas as a proxy for the off-axis lavas' initial (^{230}Th/^{232}Th) and (^{226}Ra/^{230}Th). Therefore if the off-axis lavas have been stored in the crust for a period of time significantly different than the axial lavas (either longer or shorter), their calculated U-Th and Th-Ra eruption ages could be incorrect. Because of the much shorter half-life of ^{226}Ra, this issue is potentially significant for the calculated Th-Ra ages, but it is unlikely to be important for the U-Th ages.

[31] The major and trace element compositions of several off-axis samples show that they are indeed more evolved than the axial basalts (e.g., they have lower MgO, CaO, and Al_2O_3, and higher TiO_2, K_2O, FeO, Na_2O and incompatible trace

element abundances (see e.g., Figures 3 and 4; Appendix 1)). The question is whether the residence times of these more evolved off-axis lavas were significantly longer than those of the axial lavas. Among the axial lavas from 9–10°N EPR, ^{226}Ra is negatively correlated with Mg# while ^{230}Th is positively correlated with Mg#. While samples with significant U-Th and Th-Ra ages lie below these correlations, the "zero-age" 9°50′N EPR off-axis lavas are similarly correlated (Figure 10), further confirming this functional relationship and suggesting that, relative to the half-life of ^{226}Ra, the residence times of the off-axis samples are similar to those of the axial lavas.

5. Comparison of U-Series Ages With Observational Age Constraints

[32] A number of geological features can be used to provide a gross estimate of the relative ages of submarine lava flows and to recognize eruptions that occurred away from the focus of volcanism along the AST. These features include: extent and thickness of sediment cover, thickness of Mn oxide coatings on lava surfaces, freshness of glass, lava type and morphology, stratigraphic and contact relationships, and tectonic characteristics [e.g., *Chadwick and Embley*, 1994]. The combination of U-series ages (Table 4, Figure 11), observations from submersibles and remote sensing data (Table 1, Figures 1 and 2) permits us to evaluate the relationships between U-series model ages, and geologic and geomorphologic features of the ridge crest.

[33] To a first order, there is a reasonable qualitative relationship between relative ages of our samples and the U-Th-Ra model ages determined in this study (see Tables 1 and 4, Figure 2). Samples that had the least amount of sediment cover and Mn-oxide coating, and the "freshest" and thickest glassy crusts also have the youngest U-Th and Th-Ra model ages (e.g., 2768-8; 2737-7; 2746-4; 2772-2). Samples with older model ages (e.g., 2768-3; 2746-14; 2772-3) appeared older both in the field and in hand specimen, in that they had greater amounts of sediment cover and thicker Mn-oxide coatings on thinner glassy rinds.

6. Geological and Geochemical Constraints on the Extent of Off-Axis Volcanism

[34] U-Th-Ra model ages for the 9°50′N EPR lavas analyzed in this study show a complex distribution of ages across the crestal plateau (Figure 11). Three samples (2746-9, 2746-14, and 2768-3) have U-Th and Th-Ra ages concordant with their spreading rate ages as determined from paleomagnetic data. These concordant ages suggest these samples erupted within, or close to, the AST and have since aged at a rate proportional to the crustal spreading rate. For the majority of samples, however, their U-Th-Ra model ages are younger than would be predicted by their locations and model spreading rate ages. These anomalously young ages indicate that the age of the extrusive crust is not linearly related to the time-averaged paleomagnetic spreading rate (see Figure 11c).

[35] The observational data indicate that along the 9°48′–50′N segment of the EPR crest, volcanic construction is dominated by axis-derived lobate lava flows (plus minor sheet flows), which have flowed down the upper portion of the crestal plateau. Isolated areas of off-axis eruption also contribute to volcanic construction. However, this type of volcanism is volumetrically insignificant compared to the axis-centric volcanism (Figure 1b). The U-Th-Ra ages show that these two processes are occurring contemporaneously. Samples from both sheet and lobate flows collected adjacent to the AST (e.g., 2768-8, 2746-4, 2746-7, 2771-1, 2772-2, 2772-1) and from off-axis pillow mounds (e.g., 2737-8, 2771-1, 2759-14) have anomalously young U-Th-Ra ages.

[36] For the lobate and sheet flow samples analyzed adjacent to the axis, the side scan imagery indicates that many of these flows can be traced back to the AST (Figure 1b). Sample 2768-8 typifies this type of morphology. This young sample appears to have come from a flow that originated in the AST and may have traveled as far as 1.24 kilometers off-axis. This distance is consistent with observations of the 1991 BBQ flow [*Haymon et al.*, 1993; *Gregg et al.*, 1996], which started in

the AST and has been mapped out to ~1 km off-axis. For some of the other young off-axis samples that were classified as lobate flows when they were collected, such as 2771-1, 2772-1 and 2772-2, their origin is not so apparent from the side-scan sonar images (Figure 1b). If these samples came from lava flows that originated in, or close to, the AST (as could be suggested by their flow morphologies), then one could infer from their young ages and current positions (Table 4) that they may have traveled as far as ~2 km off-axis. There are also massive flows that have older U-Th model ages. For example, sample 2746-14 has a U-Th age of 38 ± 24 ka.

[37] With regard to the pillow lavas, it is important to distinguish between breakout pillows and/or lava buds at the distal ends of lobate and sheet flows versus pillow ridges associated with off-axis faults and fissures. Samples 2768-6, 2768-3 and 2746-9 were classified as pillow lavas when they were collected. From their ages, locations and dive descriptions it is likely that these samples came from pillows and lava buds at the ends of more extensive lobate flows that originated in or adjacent to the AST (see Figure 1b and Table 1). Two of these samples (2746-9 and 2768-3) have U-Th ages that are concordant with their spreading rate ages, suggesting that they were erupted within, or close to, the AST, and have since been aging at a rate proportional to the spreading rate. However, samples 2737-8, 2759-12, and 2759-14 can be interpreted as off-axis eruptions because they come from pillow ridges mapped in the side scan imagery (Figure 1b), and are flows that were associated with faults and scarps. These samples have "zero" U-Th "model ages" but significant Th-Ra model ages (Table 4).

[38] The geochemical data indicate that 9°50′N EPR axial and off-axis lavas (measured in this study and *Sims et al.* [2002]) can be related by similar liquid lines of descent, and that their parental magmas had similar time-averaged source characteristics (as indicated by their identical radiogenic Sr, Nd, Hf and $^{208}Pb/^{206}Pb$ isotope compositions). Lavas erupted from (or close to) the AST are more primitive (higher Mg#), whereas several of the pillow ridge lavas erupted off-axis
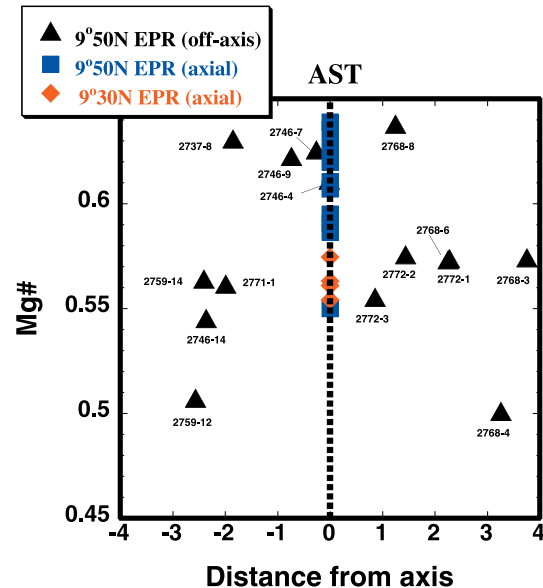
Figure 12. Mg# versus sample location, relative to the AST, for the 9°50′N EPR off-axis samples and 9–10°N EPR axial samples. The AST sample (2370-1) with the lowest Mg# (55) is from 9°47.6′N EPR, but has a composition similar to the 9°30′N EPR samples; whereas the remainder of the 9°50′N EPR axial samples have significantly higher Mg# numbers.

are more evolved (Figure 12). For example, samples 2768-8 and 2746-7 which are young and appear to be associated with lobate flows emanating from the AST, have compositions similar to the more primitive axial lavas from the 9°50N region. In contrast, samples 2759-12 and 2746-14, which were collected from pillow mounds on the west side of the AST (Figure 1), have much lower Mg#s (see Figure 12). This greater extent of differentiation for the pillow lavas erupted off-axis may indicate that they originated from colder, more distal and more differentiated portions of the axial magma lens/mush zone; alternatively, these off-axis lavas could have been derived from isolated pockets of magma, which were also colder and more differentiated [*Perfit et al.*, 1994]. Several lobate and sheet flows (e.g., 2772-3; 2768-6), which may have originated on-axis and flowed off-axis are also slightly more evolved. The greater extent of differentiation of these lavas may indicate that they came from large eruptions (hence their breaching the AST and flowing off-axis for considerable distances), which either tapped more

Table A1a. Major-Element Compositions of 9°50N EPR Off-Axis Samples[a]

Sample	SiO_2	TiO_2	Al_2O_3	FeO(total)	MnO	MgO	CaO	Na_2O	K_2O	P_2O_5	Total
2737-8	49.3	1.21	15.62	8.99	0.16	8.62	12.10	2.53	0.09	0.10	98.72
2746-4	50.4	1.36	15.28	9.43	0.18	8.32	12.10	2.64	0.11	0.15	99.96
2746-7	50.1	1.23	15.50	9.22	0.16	8.65	12.26	2.59	0.12	0.12	99.90
2746-9	50.2	1.27	15.58	9.16	0.17	8.48	12.19	2.60	0.12	0.11	99.91
2746-14	50.4	1.72	14.38	10.70	0.15	7.20	11.98	3.06	0.14	0.16	99.90
2759-12	50.7	1.95	13.86	11.74	0.20	6.78	11.23	3.00	0.16	0.19	99.81
2759-14	50.5	1.61	14.54	10.40	0.19	7.55	11.81	2.83	0.14	0.14	99.74
2768-3	50.1	1.59	14.25	10.20	0.19	7.72	11.88	2.81	0.10	0.14	98.97
2768-4	45.7	1.80	12.4	14.10	2.72	5.75	9.50	2.77	0.19	0.30	95.20
2768-6	50.0	1.60	14.21	10.28	0.17	7.75	11.81	2.68	0.11	0.13	98.73
2768-8	49.3	1.20	15.77	8.92	0.18	8.82	12.14	2.53	0.10	0.09	99.10
2771-1	49.9	1.68	14.30	10.47	0.19	7.53	11.77	2.77	0.12	0.15	98.86
2772-1	50.0	1.55	14.23	10.23	0.18	7.73	11.97	2.68	0.12	0.14	98.85
2772-2	49.7	1.52	14.21	10.10	0.17	7.69	11.95	2.67	0.12	0.14	98.28
2772-3	49.6	1.71	14.14	10.80	0.19	7.57	11.48	2.76	0.12	0.16	98.51

[a] Major-elements in weight percent, measured by Electron Microprobe at the USGS in Denver, Co. Estimated relative errors based on repeat analyses ∼2%, except for Na (5%), P (6%) and K (8%).

Table A1b. Rare-Earth Element Compositions of 9°50N EPR Off-Axis Samples Measured by ICPMS and ID-TIMS

Sample	La	Ce	Pr	Nd	Sm	Eu	Gd	Tb	Dy	Ho	Er	Yb	Lu
2737-8[a]	2.6	8.2	1.40	7.6	2.60	1.10	3.80	0.70	4.30	0.93	2.50	2.60	0.40
2737-8[b]				8.24	2.66								
2746-4[a]	2.9	9.2	1.60	8.3	2.90	1.20	4.50	0.77	4.90	1.10	2.90	2.80	0.46
2746-4[a]	3.1	9.8	1.7	9.3	3.2	1.2	4.5	0.79	5.0	1.1	2.9	3.0	0.50
2746-4[b]				7.48	2.61								
2746-7[a]	2.8	8.8	1.50	8.0	2.80	1.10	4.10	0.73	4.60	1.00	2.70	2.80	0.43
2746-9[a]	2.8	8.7	1.50	8.0	2.80	1.10	4.20	0.74	4.60	1.00	2.70	2.80	0.42
				7.97	2.78								
2746-14[a]	3.6	12.0	2.00	11.0	3.70	1.40	5.30	0.95	5.90	1.30	3.50	3.60	0.54
2746-14[b]				10.95	3.68								
2759-12[a]	4.2	14.0	2.30	13.0	4.30	1.60	6.00	1.10	6.70	1.50	4.00	4.20	0.63
2759-12[b]				12.84	4.23								
2759-14[a]	3.6	11.0	1.90	11.0	3.60	1.40	5.10	0.93	5.80	1.20	3.40	3.60	0.53
				10.84	3.53								
2768-3[c]	4.6	12.0	1.80	11.0	3.6	1.40	5.50	0.94	6.10	1.20	3.80	3.60	
2768-3[b]				9.81	3.43								
2768-4[a]	18.0	18.0	4.90	25.0	7.10	2.20	9.10	1.60	10.0	2.10	6.00	6.10	0.89
2768-4[b]				13.57	4.58								
2768-6[a]	3.4	11.0	1.90	9.9	3.40	1.40	5.20	0.93	5.70	1.30	3.40	3.40	0.56
2768-6[b]				9.95	3.44								
2768-8[a]	2.7	8.5	1.40	7.8	2.70	1.00	4.00	0.67	4.20	0.98	2.50	2.50	0.41
2768-8[b]				7.91	2.73								
2771-1[a]	3.5	11.0	1.90	11.0	3.50	1.40	5.10	0.90	5.60	1.20	3.30	3.60	0.53
2771-1[b]				10.25	3.55								
2772-1[a]	3.5	11.0	1.80	9.8	3.50	1.30	5.00	0.91	5.50	1.20	3.30	3.50	0.51
2772-1[b]				9.74	3.37								
2772-2[a]	3.5	11.0	1.90	10.0	3.50	1.30	4.90	0.89	5.60	1.20	3.30	3.50	0.51
2772-2[b]				9.74	3.37								
2772-3[a]	3.9	12.0	2.10	11.0	4.00	1.50	5.70	1.00	6.20	1.40	3.80	3.90	0.58
2772-3[b]				10.82	3.73								

[a] REE elements measured by ICPMS at Geological Survey of Canada, errors 5–10% (2 sigma).
[b] Sm and Nd concentrations measured by ID-TIMS at UC Berkeley, errors ∼1% (2 sigma).
[c] REE elements measured by ICPMS at USGS, errors 5–10% (2 sigma).

Table A1c. Cl, K, Rb, Nb, Ba, Ni, Zr, Sr, Hf and Y Concentrations of 9°50N N EPR Off-Axis Samples[a]

Sample	Cl, ppm	K, ppm	Rb, ppm	Nb, ppm	Ba, ppm	Ni, ppm	Zr, ppm	Sr, ppm	Hf, ppm	Y, ppm
2737-8	43	726	0.7	2.20	7	110	82	123	2.30	27
2746-4	39	800	0.9	2.50	8	81	92	122	2.20	30
2746-7	41	709	0.8	2.60	9	95	84	120	2.50	28
2746-9	30	727	0.8	2.50	10	98	84	120	2.40	29
2746-14			1.3	3.20	9	54	107	119	3.10	34
2759-12	85	1087	1.1	3.90	11	42	134	126	3.80	43
2759-14	64	945	0.9	3.40	9	66	109	125	3.10	35
2768-3	114	835	0.8	3.3	9		86	120	2.00	35
2768-4	782	1444	1.9	6.30	87	269	183	138	4.10	57
2768-6	132	948	1.0	3.00	10	57	102	114	2.50	34
2768-8	14	796	0.8	3.20	9	98	82	129	1.90	27
2771-1	76	976	0.9	3.20	9	67	110	126	3.00	36
2772-1	69	996	1.0	3.10	9	54	102	120	2.70	34
2772-2	81	944	1.0	3.40	10	52	102	121	3.00	35
2772-3	43	726	1.0	3.60	11	55	117	118	3.40	39

[a] Cl and K measured by electron microprobe at U of Tulsa [*Michael and Cornell*, 1998]. Errors for both Cl and K are <20 ppm (2σ). Ba measured by ID-ICPMS at WHOI and ID-TIMS at LANL. Uncertainties for both techniques <2% (2σ). Zr, Y and Sr measured by XRF at the University of Florida, errors are <4% (2σ). Rb, Nb, Ni, and Hf concentrations measured by ICPMS at Canadian Geological Survey errors ~5% (2σ).

fractionated parts of the melt lens, or erupted lavas that had longer repose periods and more time to fractionate.

7. Conclusions

[39] 1. A majority of the measured off-axis basalt samples from the 9°50 section of the EPR have U-Th and Th-Ra disequilibria that are larger, and model ages that are younger, than would be predicted from their off-axis distance and the time-integrated spreading rate. There are, however, a few off-axis samples with U-Th model ages that are consistent with their spreading rate ages. It is likely that these samples erupted within or close to the AST, and aged at a rate proportional to the spreading rate. The anomalously young model ages determined for most of the off-axis lavas and the distribution of surficial lava flows imaged by high-resolution sonar suggest that volcanic construction along the 9°–10°N EPR region is occurring over a zone that is at least ~4 km wide, considerably larger than the few hundred meter width of the actual AST.

[40] 2. Isotopic compositions of the off-axis N-MORB analyzed in this study are identical, within analytical uncertainty, to the isotopic compositions of the axial lavas from this region. Major- and trace element variations form coherent trends that can be related to the axial lavas by differing extents of fractional crystallization of similar parental magmas generated by polybaric melting.

[41] 3. The combined observational (from both submersible and remote sensing) and chemical and isotopic data support a model for the 9°50′N EPR area that includes a significant component of crustal accumulation resulting from lavas that breach the AST and flow down the flanks of the EPR ridge crest. However, these data also require a minor component of off-axis eruptions, which occur on distinct pillow mounds and ridges, as imaged by side-looking sonar data. This suggests that MOR construction at the northern EPR involves several volcanic and tectonic processes acting in concert to form a complex patchwork of lava ages and compositions along and across this fast spreading ridge crest.

Appendix A

[42] Tables showing major-element compositions of 9°50N EPR off-axis samples (Table A1a), rare-earth element compositions of 9°50N EPR off-axis samples measured by ICPMS and ID-TIMS (Table A1b), and Cl, K, Rb, Nb, Ba, Ni, Zr, Sr, Hf and Y concentrations of 9°50N N EPR off-axis samples (A1c) are given here.

Acknowledgments

References

Allegre, C. J., and M. Condomines, Basalt genesis and mantle structure studied through Th-isotopic geochemistry, *Nature*, *299*, 21–24, 1982.

Ball, L., K. Sims, S. Weyer, and J. Schwieters, Measurement of Th-232/Th-230 in volcanic rocks by PIMMS, using the ThermoFinnigan Neptune, *Geochim. Cosmochim. Acta*, *66*, A47, 2002.

Batiza, R., and Y. Niu, Petrology and magma chamber processes at the East Pacific Rise - 9°30′N, *J. Geophys. Res.*, *97*, 6779–6797, 1992.

Beattie, P., Uranium-thorium disequilibria and partitioning on melting of garnet peridotite, *Nature*, *363*, 63–65, 1993.

Blichert-Toft, J., C. Chauvel, and F. Albarède, Separation of Hf and Lu for high-precision isotope analysis of rock samples by magnetic sector-multiple collector ICP-MS, *Contrib. Mineral. Petrol.*, *127*, 248–260, 1997.

Carbotte, S. M., and K. C. Macdonald, East Pacific Rise 8°–10°30′N: Evolution of ridge segments and discontinuities from SeaMARC II and three-dimensional magnetic studies, *J. Geophys. Res.*, *97*, 6959–6982, 1992.

Chabaux, F., D. B. Othman, and J. L. Birck, A new Ra-Ba chromatographic separation and its application to Ra mass-spectrometric measurement in volcanic rocks, *Chem. Geol.*, *114*, 191–197, 1994.

Chadwick, W. W., and R. W. Embley, Lava flows from a mid-1980s submarine eruption on the cleft segment, Juan de Fuca ridge, *J. Geophys. Res.*, *99*, 4761–4776, 1994.

Christeson, G. L., G. M. Purdy, and G. J. Fryer, Structure of young upper crust at the East Pacific Rise near 9°30′N, *Geophys. Res. Lett.*, *19*, 1045–1048, 1992.

Christeson, G. L., G. M. Purdy, and G. J. Fryer, Seismic constraints on shallow crustal emplacement processes at the fast-spreading East Pacific Rise, *J. Geophys. Res.*, *99*, 17,957–17,973, 1994.

Christeson, G. L., G. M. Kent, G. M. Purdy, and R. S. Detrick, Extrusive thickness variability at the East Pacific Rise, 9°–10°N, constraints from seismic techniques, *J. Geophys. Res.*, *101*, 2859–2873, 1996.

Cochran, J. R., D. J. Fornari, B. J. Coakley, R. Herr, and M. A. Tivey, Continuous near-bottom gravity measurements made with a BGM-3 gravimeter in DSV Alvin on the East Pacific Rise crest near 9°30′N and 9°50′N, *J. Geophys. Res.*, *104*, 10,841–10,861, 1999.

Cohen, A. S., and R. K. O'Nions, Precise determination of femtogram quantities of radium by thermal ionization mass spectrometry, *Anal. Chem.*, *63*, 2705–2708, 1991.

Cooper, K., S. J. Goldstein, K. W. W. Sims, and M. T. Murrell, Uranium-series chronology of Gorda Ridge volcanism: New evidence from the 1996 eruption, *Earth Planet. Sci. Lett.*, *206*, 459–475, 1996.

DePaolo, D. J., *Neodymium Isotope Geochemistry*, Springer-Verlag, New York, 1988.

Detrick, R. S., P. Buhl, E. Vera, J. Orcutt, J. Madsen, and T. Brocher, Multi-channel seismic imaging of a crustal magma chamber along the East Pacific Rise, *Nature*, *326*, 35–41, 1987.

Fornari, D., R. Haymon, M. Perfit, T. K. P. Gregg, and M. H. Edwards, Axial summit trough of the East Pacific Rise, 9°–10°N: Geological characteristics and evolution of the axial zone on fast spreading mid-ocean ridges, *J. Geophys. Res.*, *103*, 9827–9855, 1998.

Goldstein, S. J., M. T. Murrell, and D. R. Janecky, Th and U isotopic systematics of basalts from the Juan de Fuca and Gorda Ridges by mass spectrometry, *Earth Planet. Sci. Lett.*, *96*, 134–146, 1989.

Goldstein, S. J., M. T. Murrell, D. R. Janecky, J. R. Delaney, and D. Clague, Geochronology and petrogenesis of MORB from the Juan de Fuca and Gorda Ridges by ^{238}U-^{230}Th disequilibrium, *Earth Planet. Sci. Lett.*, *107*, 25–41, 1991. (Erratum, *Earth Planet. Sci. Lett.*, *109*, 255–272, 1992.)

Goldstein, S. J., M. T. Murrell, and R. W. Williams, ^{231}Pa and ^{230}Th chronology of mid-ocean ridge basalts, *Earth Planet. Sci. Lett.*, *115*, 151–160, 1993.

Goldstein, S. J., M. R. Perfit, R. Batiza, D. J. Fornari, and M. T. Murrell, Off-axis volcanism at the East Pacific Rise detected by uranium-series dating of basalts, *Nature*, *367*, 157–159, 1994.

Gregg, T. K. P., D. F. Fornari, M. P. Perfit, R. M. Haymon, and J. H. Fink, Rapid emplacement of a mid-ocean ridge lava flow on the East Pacific Rise at 9°46′–51′N, *Earth Planet. Sci. Lett.*, *144*, E1–E7, 1996.

Harding, A. J., G. M. Kent, and J. A. Orcutt, A multichannel seismic investigation of upper crustal structure at 9°N on the East Pacific Rise: Implications for crustal accretion, *J. Geophys. Res.*, *98*, 13,925–13,944, 1993.

Haymon, R. M., D. J. Fornari, M. H. Edwards, S. C. Carbotte, D. Wright, and K. C. Macdonald, Hydrothermal vent distribution along the East Pacific Rise Crest (9°09′–54′N) and its

relationship to magmatic and tectonic processes on fast-spreading mid-ocean ridges, *Earth Planet. Sci. Lett.*, *104*, 513–534, 1991.

Haymon, R., et al., Volcanic eruption of the mid-ocean ridge along the East Pacific at 9°45–52′N: I. Direct submersible observation of sea floor phenomena associated with an eruption event in April, 1991, *Earth Planet. Sci. Lett.*, *119*, 85–101, 1993.

Hooft, E. E. E., H. Schouten, and R. S. Detrick, Constraining crustal emplacement processes from the variation in seismic layer 2A thickness at the East Pacific Rise, *Earth Planet. Sci. Lett.*, *142*, 289–309, 1996.

Jull, M., P. Kelemen, and K. W. W. Sims, Melt migration and uranium series disequilibria: The combined effect of porous and conduit flow, *Geochim. Cosmochim. Acta.*, *66*, 4133–4148, 2003.

Ku, T.-L., K. G. Knauss, and G. G. Mathieu, Uranium in open ocean: Concentration and isotopic composition, *Deep Sea Res.*, *1977*, 1005–1017, 1977.

Kurras, G. J., D. J. Fornari, M. H. Edwards, M. J. Perfit, and M. C. Smith, Volcanic morphology of the East Pacific Rise Crest 9°49–52′: Implications for volcanic emplacement processes at fast-spreading mid-ocean ridges, *Mar. Geophys. Res.*, *21*, 23–41, 2000.

Landwehr, D., J. Blundy, E. M. Chamorro-Perez, E. Hill, and B. Wood, U-series diisequilibria generated by partial melting of spinel lherzolite, *Earth Planet Sci. Lett.*, *188*, 329–348, 2001.

Langmuir, C. H., J. F. Bender, and R. Batiza, Petrological segmentation of the East Pacific Rise, 5°30′–14°30′N, *Nature*, *322*, 422–429, 1986.

LaTourrette, T. Z., A. K. Kennedy, and G. J. Wasserburg, U-Th fractionation by garnet-evidence for a deep source and rapid rise by oceanic basalts, *Science*, *261*, 739–742, 1993.

Layne, G. D., and K. W. Sims, Secondary Ion Mass Spectrometry for the measurement of ^{232}Th/^{230}Th in volcanic rocks, *Int. J. Mass Spect.*, *203*, 187–198, 2000.

Lundstrom, C. C., J. Gill, Q. Williams, and M. R. Perfit, Mantle melting and basalt extraction by equilibrium porous flow, *Science*, *270*, 1958–1961, 1995.

Lundstrom, C. C., D. E. Sampson, M. R. Perfit, J. Gill, and Q. Williams, Insights into mid-ocean ridge basalt petrogenesis: U-series disequilibria from the Siqueiros Transform, Lamont Seamounts, and East Pacific Rise, *J. Geophys. Res.*, *104*, 13,035–13,048, 1999.

Lundstrom, C. C., Q. Williams, and J. Gill, A geochemically consistent hypothesis for MORB generation, *Chem. Geol.*, *162*, 105–126, 2000.

Macdonald, K. C., and P. J. Fox, The axial summit graben and cross-sectional shape of the East Pacific Rise as indicators of axial magma chambers and recent volcanic eruption, *Earth Planet. Sci. Lett.*, *88*, 119–131, 1988.

Macdonald, K. C., P. J. Fox, R. T. Alexander, R. Pockalny, and P. Gente, Volcanic growth faults and the origin of Pacific abyssal hills, *Nature*, *380*, 125–129, 1996.

McDonough, W. M., and S.-S. Sun, The composition of the Earth, *Chem. Geol.*, *120*, 223–253, 1995.

McKenzie, D., ^{230}Th-^{238}U disequilibrium and the melting processes beneath ridge axes, *Earth Planet. Sci. Lett.*, *72*, 149–157, 1985.

Michael, P. J., and W. C. Cornell, Influence of spreading rate and magma supply on crystallization and assimilation beneath mid-ocean ridges: Evidence from chlorine and major-element chemistry of mid-ocean ridge basalts, *J. Geophys. Res.*, *103*, 18,325–18,356, 1998.

Perfit, M. R., and W. W. Chadwick Jr., Magmatism at mid-ocean ridges: Constraints from volcanological and geochemical investigations, in *Faulting and Magmatism at Mid-Ocean Ridges*, edited by W. R. Buck et al., pp. 41–70, AGU, Washington, D.C., 1998.

Perfit, M., D. Fornari, M. Smith, J. Bender, C. Langmuir, and R. Haymon, Small-scale spatial and temporal variations in MORB geochemistry and implications for ridge crest magmatic processes, *Geology*, *22*, 375–379, 1994.

Perfit, M. R., et al., Recent volcanism in the siqueiros transform fault: Picritic basalts and implications for MORB magma genesis, *Earth Planet. Sci. Lett.*, *141*, 61–73, 1996.

Reynolds, J. R., and C. H. Langmuir, Identification and implications of off-axis lava flows around the East Pacific Rise, *Geochem. Geophys. Geosyst.*, *1*, Paper number 1999GC000033, 2000.

Rubin, K. H., and J. D. MacDougall, Dating of neovolcanic MORB using (^{226}Ra/^{230}Th) disequilibrium, *Earth. Planet. Sci. Lett.*, *101*, 313–321, 1990.

Rubin, K., J. D. Macdougall, and M. R. Perfit, ^{210}Po-^{210}Pb dating of recent volcanic eruptions on the sea floor, *Nature*, *368*, 841–844, 1994.

Saal, A. E., J. A. Van Orman, E. H. Hauri, C. H. Langmuir, and M. R. Perfit, An alternative hypothesis for the origin of the high Ra-226 excess in mid-ocean ridge basalts, *Geochim. Cosmochim. Acta*, *66*, A659, 2002.

Scheirer, D. S., and K. C. Macdonald, Variation in cross-sectional area of the axial ridge along the East Pacific Rise: Evidence for the magmatic budget of a fast spreading center, *J. Geophys. Res.*, *98*, 22,321–22,338, 1993.

Scheirer, D. S., D. J. Fornari, S. E. Humphris, and S. Lerner, High-resolution seafloor mapping using the DSL-120 sonar system: Quantitative assessment of side-scan and phase-bathymetry data from the Lucky Strike segment of the Mid-Atlantic Ridge, *Mar. Geophys. Res.*, *21*, 121–142, 2000.

Schouten, H., M. A. Tivey, D. J. Fornari, and J. R. Cochran, Central Anomaly Magnetization High: Constraints on the volcanic construction and architecture of seismic layer 2A at a fast-spreading Mid-Ocean Ridge, the EPR at 9°30′–50′N, *Earth Planet. Sci. Lett.*, *169*, 37–50, 1999.

Schouten, H., M. Tivey, D. Fornari, D. Yoeger, A. Bradley, M. Edwards, P. Johnson, and Ship Board Science and Technical Teams, Near-Bottom Investigations of the Central Anomaly Magnetic High (CAMH) at the Aest Pacific Rise 9°25′–57N, Cruise Report R/V Atlantis Voyage 7 Leg 4, 11/05–12/04/2001, 2001. (Available at http://imina.soest.hawaii.edu/HMRG/EPR/index.htm)

Schouten, H., M. Tivey, D. Fornari, D. Yoerger, A. Bradley, P. Johnson, M. Edwards, and T. Kurokawa, Lava transport

and accumulation processes on EPR 9 27′N to 10N: Interpretations based on recent near-bottom sonar imaging and seafloor observations using ABE, Alvin and a new digital deep sea camera, *Eos Trans. AGU*, *83*(47), Fall Meet. Suppl., Abstract T11C-1262, 2002.

Sims, K. W. W., D. J. DePaolo, M. T. Murrell, W. S. Baldridge, S. J. Goldstein, and D. A. Clague, Mechanisms of magma generation beneath Hawaii and mid-ocean ridges: U/Th and Sm/Nd isotopic evidence, *Science*, *267*, 508–512, 1995.

Sims, K. W. W., D. J. DePaolo, M. T. Murrell, W. S. Baldridge, and S. J. Goldstein, Porosity of the melt zone and variations in solid mantle upwelling rates beneath Hawaii: Inferences from ^{238}U-^{230}Th-^{226}Ra and ^{235}U-^{231}Pa Disequilibria, *Geochim. Cosmchim. Acta.*, *63*, 4119–4138, 1999.

Sims, K. W. W., et al., Chemical and isotopic constraints on the generation and transport of melt beneath the East Pacific Rise, *Geochim. Cosmchim. Acta.*, *66*, 3481–3504, 2002.

Smith, M. C., M. R. Perfit, D. J. Fornari, W. I. Ridley, M. H. Edwards, G. J. Jurras, and K. L. Von Damm, Magmatic processes and segmentation at a fast spreading mid-ocean ridge; detailed investigation of an axial discontinuity on the East Pacific Rise crest at 9 degrees 37′N, *Geochem. Geophys. Geosyst.*, *2*, Paper 2000GC000134, 2001.

Spiegelman, M., and T. Elliott, Consequences of melt transport for uranium series disequilibrium in young lavas, *Earth Planet. Sci. Lett.*, *118*, 1–20, 1993.

Thurber, D., Anamolous $^{234}U/^{238}U$ in nature, *J. Geophys. Res.*, *67*, 4518, 1962.

Todt, W., R. A. Cliff, A. Hanser, and A. W. Hofmann, Evaluation of a 202Pb-205Pb double spike for high-precision lead isotope analysis, in *Earth Processes Reading the Isotopic Code*, vol. 95, edited by S. R. Hartand and A. Basu, pp. 429–437, AGU, Washington, D.C., 1996.

Vera, E. E., and J. B. Diebold, Seismic imaging of oceanic layer 2A between 9°30 and 10°N on the East Pacific Rise from two ship wide-aperature profiles, *J. Geophys. Res.*, *99*, 3031–3041, 1994.

Volpe, A. M., and S. J. Goldstein, ^{226}Ra-^{230}Th Disequilibrium in Axial and Off-Axis Mid-Ocean Ridge Basalts, *Geochim. Cosmochim. Acta.*, *57*, 1233–1242, 1993.

Volpe, A. M., J. A. Olivares, and M. T. Murrell, Determination of radium isotope ratios and abundances in geologic samples by thermal ionization mass spectrometry, *Anal. Chem.*, *63*, 913–916, 1991.

White, S. M., R. M. Haymon, D. J. Fornari, M. R. Perfit, and K. C. Macdonald, Correlation between volcanic and tectonic segmentation of fast-spreading ridges: Evidence from volcanic structures and lava flow morphology on the East Pacific Rise at 9–10N, *J. Geophys. Res.*, *107*(B8), doi:10.1029/2002GC000443, 2002.

White, W. M., F. Albarède, and P. Télouk, High-precision analysis of Pb isotope ratios using multi-collector ICP-MS, *Chem. Geol.*, *167*, 257–270, 2000.

Williams, R. W., and J. B. Gill, Effects of partial melting on the uranium decay series, *Geochim. Cosmochim. Acta.*, *53*, 1607–1619, 1989.